Article

Cell

Adrenergic Signaling in Muscularis Macrophages Limits Infection-Induced Neuronal Loss

Graphical Abstract

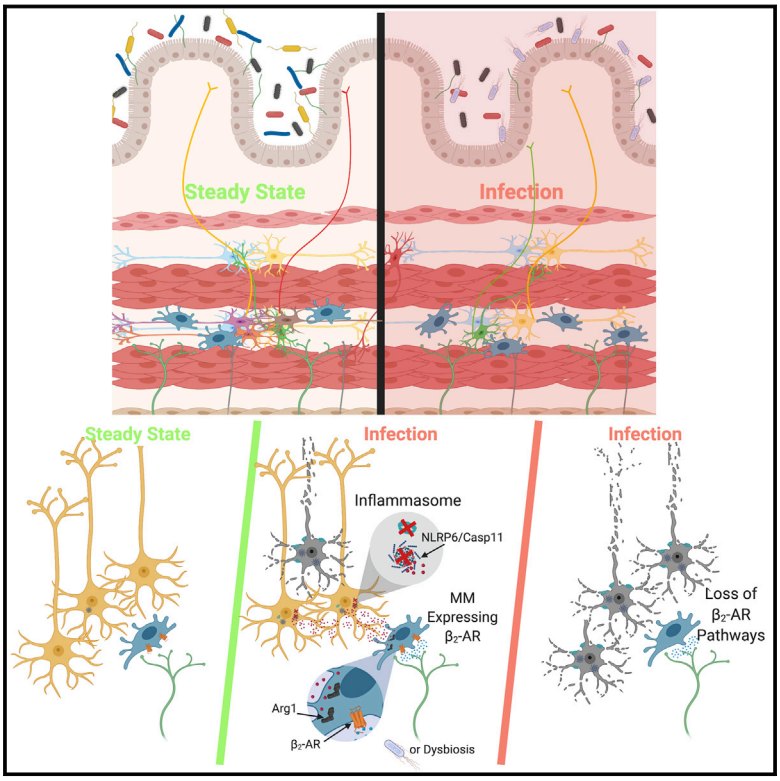

Authors

Fanny Matheis, Paul A. Muller, Christina L. Graves, ..., Tomasz Ahrends, Philip Rosenstiel, Daniel Mucida

Correspondence

pmuller@rockefeller.edu (P.A.M.), mucida@rockefeller.edu (D.M.)

In Brief

Bacterial enteric infections lead to lasting inflammatory changes in the intestine with concomitant reduction in the myenteric neuron number caused by *Nlrp6*- and *caspase 11*-mediated cell death, which can be opposed by β2-adrenergic-arginase 1-polyamine axis signaling in *muscularis* macrophages.

Highlights

- Enteric pathogens trigger reversible neuronal loss and long-term GI symptoms
- Enteric infection-triggered neuronal loss is *Nlrp6*- and *caspase 11*-dependent
- Intestinal *muscularis* macrophages (MMs) rapidly respond to enteric pathogens
- Neuronal death is limited by a MM-β_2-adrenergic-arginase 1-polyamine axis

Data resources

GSE140309

Matheis et al., 2020, Cell *180*, 64–78
January 9, 2020
https://doi.org/10.1016/j.cell.2019.12.002

CellPress

Cell

Article

Adrenergic Signaling in Muscularis Macrophages Limits Infection-Induced Neuronal Loss

Fanny Matheis,[1,6] Paul A. Muller,[1,6,*] Christina L. Graves,[1,3] Ilana Gabanyi,[1,4] Zachary J. Kerner,[1] Diego Costa-Borges,[1,5] Tomasz Ahrends,[1] Philip Rosenstiel,[2] and Daniel Mucida[1,7,*]

[1]Laboratory of Mucosal Immunology, The Rockefeller University, New York, NY 10065, USA
[2]Institute of Clinical Molecular Biology, Kiel University and University Hospital Schleswig-Holstein, Campus Kiel, Kiel 24105, Germany
[3]Present address: Department of Biology, University of North Carolina at Chapel Hill, Chapel Hill, NC 27599, USA
[4]Present address: Department of Immunology, Institut Pasteur, Paris 75015, France
[5]Present address: Departamento de Bioquímica e Imunologia, Universidade Federal de Minas Gerais, Belo Horizonte, MG 31270901, Brazil
[6]These authors contributed equally
[7]Lead Contact
*Correspondence: pmuller@rockefeller.edu (P.A.M.), mucida@rockefeller.edu (D.M.)
https://doi.org/10.1016/j.cell.2019.12.002

SUMMARY

Enteric-associated neurons (EANs) are closely associated with immune cells and continuously monitor and modulate homeostatic intestinal functions, including motility and nutrient sensing. Bidirectional interactions between neuronal and immune cells are altered during disease processes such as neurodegeneration or irritable bowel syndrome. We investigated the effects of infection-induced inflammation on intrinsic EANs (iEANs) and the role of intestinal *muscularis* macrophages (MMs) in this context. Using murine models of enteric infections, we observed long-term gastrointestinal symptoms, including reduced motility and loss of excitatory iEANs, which was mediated by a *Nlrp6*- and *Casp11*-dependent mechanism, depended on infection history, and could be reversed by manipulation of the microbiota. MMs responded to luminal infection by upregulating a neuroprotective program via β_2-adrenergic receptor (β_2-AR) signaling and mediated neuronal protection through an arginase 1-polyamine axis. Our results identify a mechanism of neuronal death post-infection and point to a role for tissue-resident MMs in limiting neuronal damage.

INTRODUCTION

The gastrointestinal (GI) tract comprises the largest environmental interface of the body and is posed with the unique challenge of maintaining tolerance to dietary and microbial antigens while protecting against pathogen invasion. Coordinated tolerance and resistance mechanisms serve to prevent pathogen dissemination, limit GI damage, and initiate repair responses induced by pathogenic burden or injury (Medzhitov et al., 2012). In the GI tract, infections can result in functional GI disorders post-pathogen clearance, and often, enteric neurons—which occupy the intestinal tissue in large numbers—are targeted (Balemans et al., 2017). Clinical observations indicate that between 6%–17% of individuals with irritable bowel syndrome (IBS) develop symptoms after episodes of enteric infections, while around 10% of people with bacterial gastroenteritis develop IBS (Holschneider et al., 2011; Ohman and Simrén, 2010). Further, HSV-1 and flavivirus strains with neuronal tropism, including West Nile and Zika viruses, have also been reported to induce long-term intestinal dysmotility (Khoury-Hanold et al., 2016; White et al., 2018). The clinical presentation of post-infectious IBS includes unresolved low-grade intestinal inflammation, GI motility impairment, and nerve damage (Beatty et al., 2014; Holschneider et al., 2011). However, the underlying mechanisms involved in infection-induced neuronal damage are incompletely understood.

The intestinal immune and nervous systems sense and integrate luminal cues and regulate physiological processes, including GI motility. Recent evidence suggests that intestinal-resident macrophage populations play a role in normal functioning of enteric neurons in the absence of infections (De Schepper et al., 2018; Muller et al., 2014). Specifically, *muscularis* macrophages (MMs), located within and surrounding the myenteric plexus, were shown to regulate the activity of enteric neurons and peristalsis via secretion of BMP2 in a microbiota-dependent manner (Muller et al., 2014). Additionally, we previously reported that MMs displayed a tissue-protective gene expression profile, a signature that was enhanced following enteric infection, and involved β_2-adrenergic receptor (β_2-AR) signaling (Gabanyi et al., 2016). It remained to be determined, however, whether this neuron-macrophage crosstalk plays a role in infection-induced neuronal damage, or prevention thereof.

By utilizing imaging, cell-sorting-independent transcriptomics, pharmacological and genetic gain- and loss-of-function approaches, surgical lesioning, and chemogenetic manipulations, we report that murine enteric infections result in a rapid and persistent loss of intrinsic enteric-associated neurons (iEANs), which is associated with long–term GI changes including intestinal dysmotility, via the non-canonical inflammasome components *Nlrp6* and *Casp11*. Myeloid-specific targeting of β_2-AR, as well as arginase 1 (Arg1), coupled with

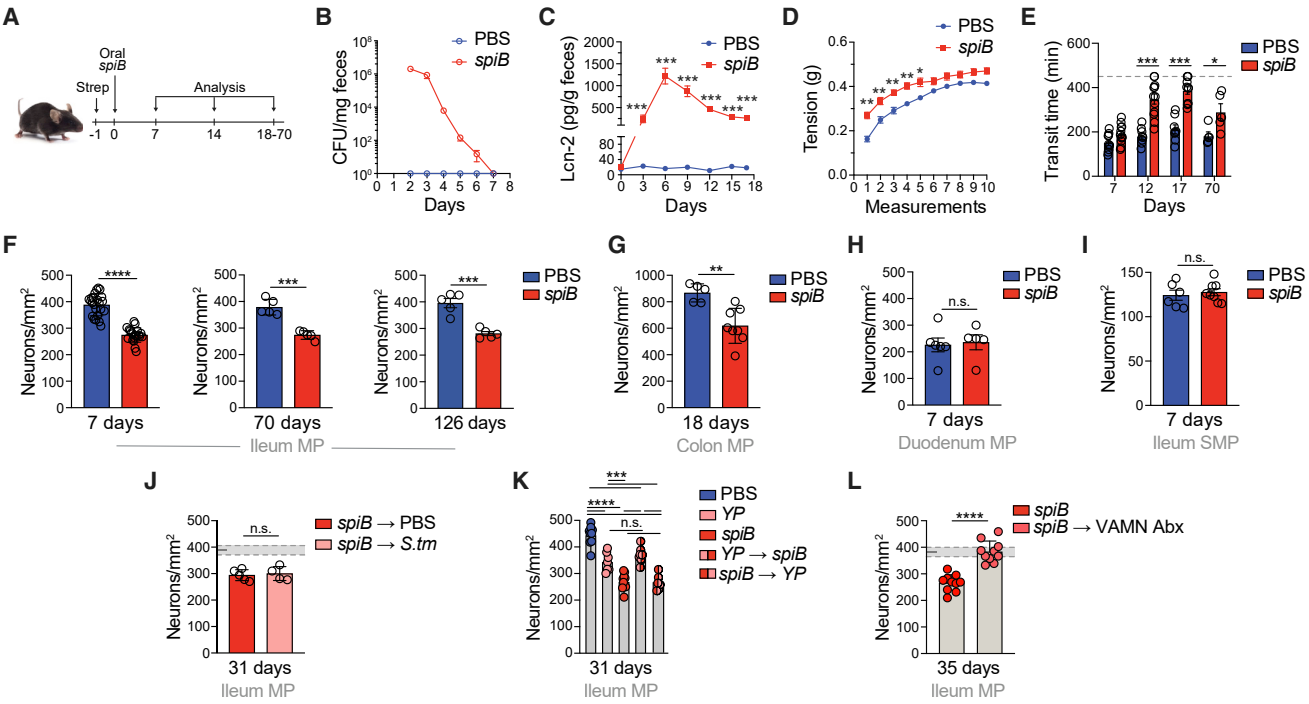

Figure 1. Enteric Infections Trigger Intrinsic Neuronal Loss and Dysmotility

(A) Experimental design for (B–I).

(B–H) C57BL/6J mice were orally gavaged with PBS or 10^9 colony-forming units (CFU) of *Salmonella spiB*.

(B) Quantification of fecal CFU.

(C) Quantification of fecal lipocalin-2 (Lcn-2) levels as assessed by ELISA post-infection.

(D) Ileal ring myography assessed on day 18 post-infection.

(E) Total GI transit time. Experiments were ended at 450 min (dashed line)

(F–I) Neuronal quantification as assessed by IF staining (ANNA-1) on the indicated days post-infection in the ileum (F), colon (G), duodenum MP (H), and ileum SMP (I).

(J) Neuronal quantification (ANNA-1 staining) in the ileum myenteric plexus of C57BL/6J mice orally gavaged PBS or WT *Salmonella* Typhimurium (*S. tm*) 21 days post-*spiB* infection and sacrificed on day 10 post-re-infection. Shaded area indicates mean day 7 iEAN numbers ± SEM of all control C57BL6/J mice (F).

(K) Neuronal quantification in the ileum myenteric plexus of C57BL/6J mice orally gavaged with PBS, *Y. pseudotuberculosis* (*YP*), *spiB* or *spiB* or *YP* followed by infection with *YP* or *spiB*, respectively, and sacrificed 10 days post-secondary infection.

(L) Neuronal quantification in the ileum myenteric plexus of C57BL/6J mice reconstituted with a normal microbiota or not after *spiB* infection.

Abbreviations are as follows: MP, Myenteric plexus; SMP, Submucosal plexus. Data are representative of at least 5 mice per condition. Data were analyzed by unpaired t test or ANOVA with Tukey's post-hoc test and are shown as mean ± SD; n.s. - not significant; *p ≤ 0.05, **p ≤ 0.01, ***p ≤ 0.001, ****p ≤ 0.0001. See also Figure S1.

pharmacological rescue experiments and exogenous activation of gut-sympathetic neurons implicated MM-adrenergic signaling in post-infectious enteric neuronal protection via production of polyamines. Our data uncover a novel mechanism of enteric neuronal cell death and identify a functional role for neuron-macrophage interactions in limiting infection-induced neuronal damage.

RESULTS

Enteric Pathogens Trigger Long-Term Impairment in GI Physiology

Acute bacterial infections, including *Salmonella enterica* serovar Typhimurium, *Shigella dysenteriae*, and *Campylobacter spp.*, have previously been linked to post-infectious IBS (Ohman and Simrén, 2010). To characterize functional consequences of acute bacterial infection in mice, we used an attenuated strain of *S.* Typhimurium, *spiB* (Tsolis et al., 1999), which harbors a mutation in the type III secretion system, impacting its intracellular replication. We chose to use *spiB* because wild-type (WT) *S.* Typhimurium rapidly invades and damages the intestinal wall, resulting in mortality in WT C57BL/6 mice, thus barring long-term functional studies post-pathogen clearance. We observed that orally administered *spiB* was undetected in the feces by 7–10 days post-infection (dpi) (Figures 1A and 1B). Infection with *spiB* caused mild intestinal inflammation as evidenced by increased levels of fecal lipocalin-2 (Lcn-2), which remained elevated after pathogen clearance (Figure 1C). This persistent inflammatory response was associated with lasting GI functional changes, including increased ileal ring contractility and a persistent delay in GI transit time (GITT) (Figures 1D and 1E).

Changes in contractility and GITT can be associated with altered neuronal activity and nerve damage (Travagli and

Anselmi, 2016). iEANs, commonly referred to as the enteric nervous system, are organized in two distinct networks: the submucosal or Meissner's and myenteric or Auerbach's plexuses (Furness et al., 2013). In order to determine the impact of intestinal infection on iEANs, we quantified enteric neurons along the GI tract in both the submucosal and myenteric plexuses. Following *spiB* infection, we observed a 20%–30% reduction in myenteric neurons 7 dpi in the ileum and colon, both of which are major sites of *Salmonella* invasion; reduced neuronal counts were observed up to 126 dpi (Figures 1F and 1G). In contrast, neuronal numbers were preserved in the proximal small intestine, where *Salmonella* invasion normally does not occur, and the submucosal plexus; additionally, heat-killed *spiB* did not result in myenteric iEAN loss (Figures 1H–1I and S1A). Loss of iEANs was also observed after infection with another enteric bacterial pathogen, *Yersinia pseudotuberculosis* (Figure S1B). We further interrogated whether we could recapitulate our findings in the context of the clinically relevant protozoan pathogens *Toxoplasma gondii* and *Trypanosoma cruzi*, which are known to induce GI-related pathologies (Dutra et al., 2009). These protozoans also induced intestinal inflammation, increased ileal ring contractility, delayed GITT, and significant neuronal loss (Figures S1C–S1G) (data not shown). By contrast, infection with the intestinal helminth *Strongyloides venezuelensis*, which displays distinct duodenal tropism (Esterházy et al., 2019), did not lead to iEAN loss in either the proximal or distal intestine (Figure S1H). Together, these data indicate that iEAN loss may be a conserved feature of many, though not all, enteric infections; we chose to continue with *spiB* as an infection model because of the inherent neurotropism of *T. gondii* and *T. cruzi*.

While it is traditionally thought that mammalian enteric neurogenesis ceases postnatally, recent studies suggest continuous turnover of iEANs, for instance, by replenishment from Nestin+ stem cells (Kulkarni et al., 2017). However, in the present study, we were not able to detect iEAN number recovery up to four months after *spiB* clearance nor observe changes in *Nestin*$^{GFP+}$ cell networks in the myenteric plexus (Figure S1I). As an orthogonal approach, we evaluated the involvement of enteric glia, which have been shown to replenish iEANs in response to injury (Laranjeira et al., 2011), in neuronal maintenance after *spiB* infection. Using an inducible *Sox10*^{RiboTag} fate mapping strategy, we found that approximately 10% of iEANs were hemagglutinin positive (HA+) four months following tamoxifen administration to adult *Sox10*^{RiboTag} control mice, suggesting a glial origin of these cells. However, we did not observe iEAN recovery nor changes in the frequency of HA+ cells in the ileum myenteric plexus of *Sox10*^{RiboTag} mice infected with *spiB* in the same period of time (Figure S1J). These results indicate that without further manipulations, iEAN loss is persistent in this model of infection.

Given the significant reduction in ileal and colonic myenteric neurons resulting from a single *spiB* infection, we asked whether subsequent infections would exacerbate iEAN damage. Following clearance of *spiB,* we infected mice with WT *Salmonella*, after which we observed no additional iEAN loss. This indicates a possible restructuring or adaptation of tissue cells preventing further damage (Figure 1J). To exclude the contribution of adaptive immunological memory, we performed infection challenge with *spiB* and *Y. pseudotuberculosis*, bacterial pathogens that resulted in iEAN loss post-primary infections. Primary infection with *Y. pseudotuberculosis* resulted in iEAN protection against secondary challenge with *spiB*, and conversely, initial iEAN loss with primary *spiB* infection was not enhanced with subsequent *Y. pseudotuberculosis* infection (Figure 1K). The above results demonstrate that infections with different enteric pathogens induce prolonged low-grade inflammation and GI dysmotility, which are associated with a rapid and self-limiting, yet persistent loss of iEANs.

Human post-infectious IBS generally leads to long-term, but reversible GI symptoms and neuropathy (Beatty et al., 2014; Ohman and Simrén, 2010). However, here, we did not observe recovery of neurons after a single infection. Because of reported effects of microbiota on the development and maintenance of enteric neurons, including recent work from our group (Muller et al., 2019; Obata and Pachnis, 2016), we assessed whether persistent changes in microbial composition (dysbiosis) could explain the lack of iEAN recovery post-infection. We infected specific pathogen-free (SPF) mice with *spiB*, administered broad-spectrum antibiotics after bacterial clearance, and subsequently re-colonized the animals with SPF microbiota. This reconstitution of a "normal" or pre-infection microbiota allowed for iEAN recovery, effects that were correlated with a reduction in a member of the *Erysipelotrichaceae* family and Bacteriodales order when compared with untreated-infected mice (Figures 1L, S1K, and S1L). These data point to a role for the gut microbiota in the recovery of iEANs post-infection.

Enteric Infection-Induced Neuronal Loss is Subtype Specific

iEANs comprise a numerous and heterogeneous population of neurons that monitor and respond to various environmental cues, including mechanical stretch and luminal metabolites (Furness et al., 2013). We first asked whether the observed loss of iEANs could be explained by a decrease of ELAVL3/4 protein expression. We interbred pan-neuronal *Snap25*^{Cre} with *Rpl22*$^{lsl-HA}$ (RiboTag) mice (Sanz et al., 2009), which express a HA-tagged ribosomal subunit 22. Immunofluorescence (IF) analysis of HA+ cells in the myenteric plexus confirmed identical loss of iEANs previously determined by ANNA-1 staining (Figure 2A) (Muller et al., 2019). In cases of overt intestinal inflammation, an indiscriminate loss of iEANs have previously been reported (Mawe, 2015). In the case of enteric infection, to investigate whether specific neuronal subsets were preferentially lost, we used confocal IF imaging to evaluate the impact on excitatory and inhibitory iEAN populations (Zeisel et al., 2018). Imaging of the ileum myenteric plexus from *Slc17a6*$^{td-Tomato}$ (VGLUT2) reporter mice revealed a significant reduction in the total number and percentage of excitatory VGLUT2+ neurons post-*spiB* infection (Figure 2B). In contrast, quantification of inhibitory neuronal nitric oxide synthase-positive (nNOS+) and somatostatin-positive (SST+) iEANs revealed no changes and a relative increase post-infection, respectively (Figures 2C, 2D, S2A, and S2B). These data suggest a preferential loss of excitatory neuronal subsets post-infection, resulting in changes in the neurochemical representation of iEANs, and may provide an explanation for the observed GI functional changes.

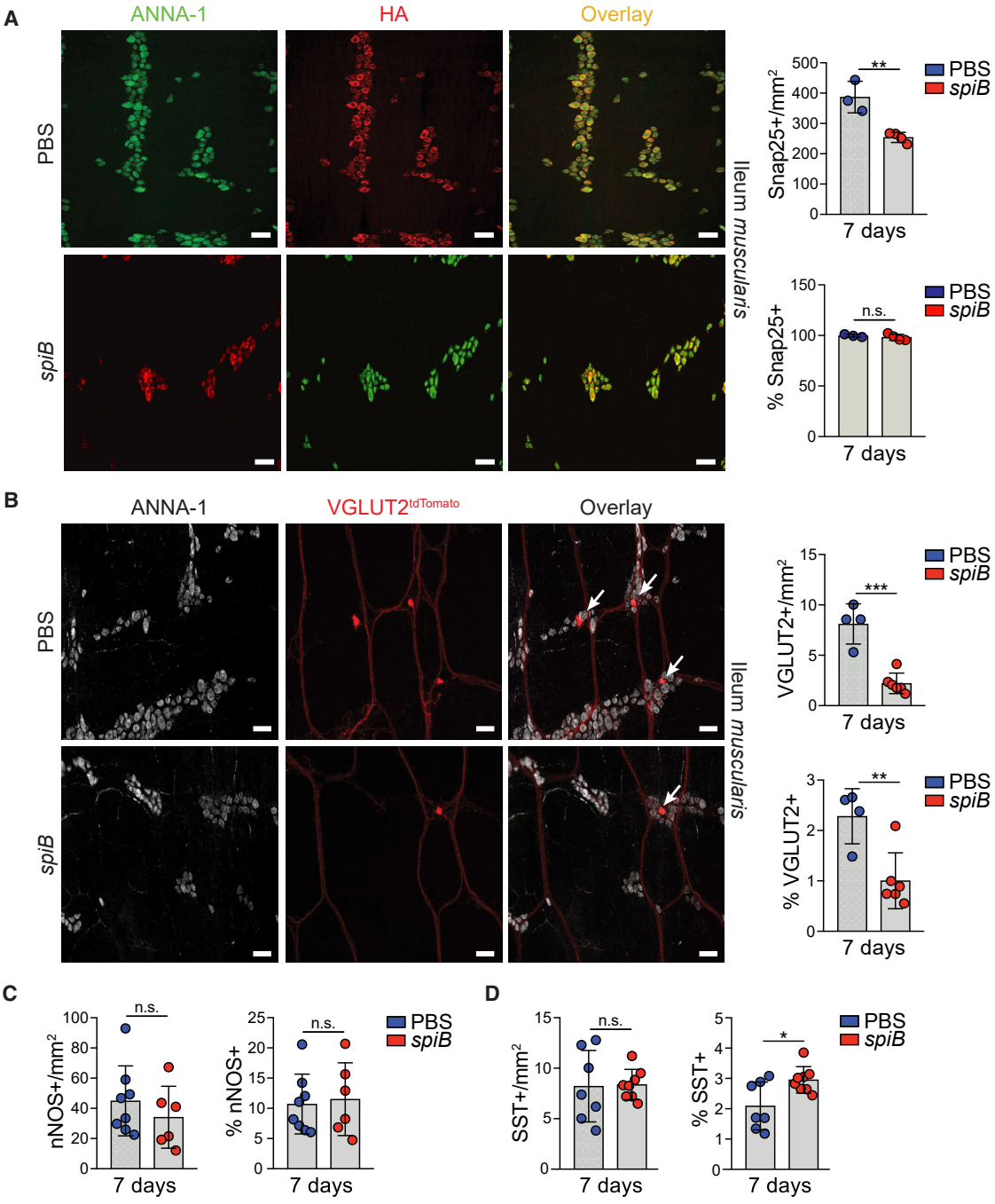

Figure 2. Enteric Infections Cause Subtype-Specific Neuronal Loss

(A–D) Mice were orally gavaged with PBS or *spiB* and analyzed 7 dpi.

(A) Left: representative confocal IF images of the ileum myenteric plexus stained with anti-ANNA-1 (red) and anti-HA (green) from *Snap25*^{RiboTag} mice treated with (top) PBS or infected with (bottom) *spiB*. Scale bars, 50 μm. Images representative of at least n = 3 per condition. Right: quantification of the (top) number of HA+ neurons per mm^2 or (bottom) percent HA/ANNA-1 overlap.

(B) Left: representative confocal IF image of the ileum myenteric plexus stained with anti-ANNA-1 (gray) from VGLUT2$^{td\text{-}Tomato}$ mice treated with (top) PBS or infected with (bottom) *spiB*. Scale bars, 50 μm. Images representative of at least n = 4 per condition. Right: quantification of the number of VGLUT2+ neurons per mm^2 and as a percentage of ANNA-1+ neurons.

(C and D) Quantification of the number of (C) nNOS+ and (D) SST+ neurons per mm^2 and as a percentage of ANNA-1+ neurons.

Data are representative of at least 3 mice per condition. Data were analyzed by unpaired Student's t test and are shown as mean ± SD; *p ≤ 0.05, **p ≤ 0.01, ***p ≤ 0.001.

See also Figure S2 and Data S1.

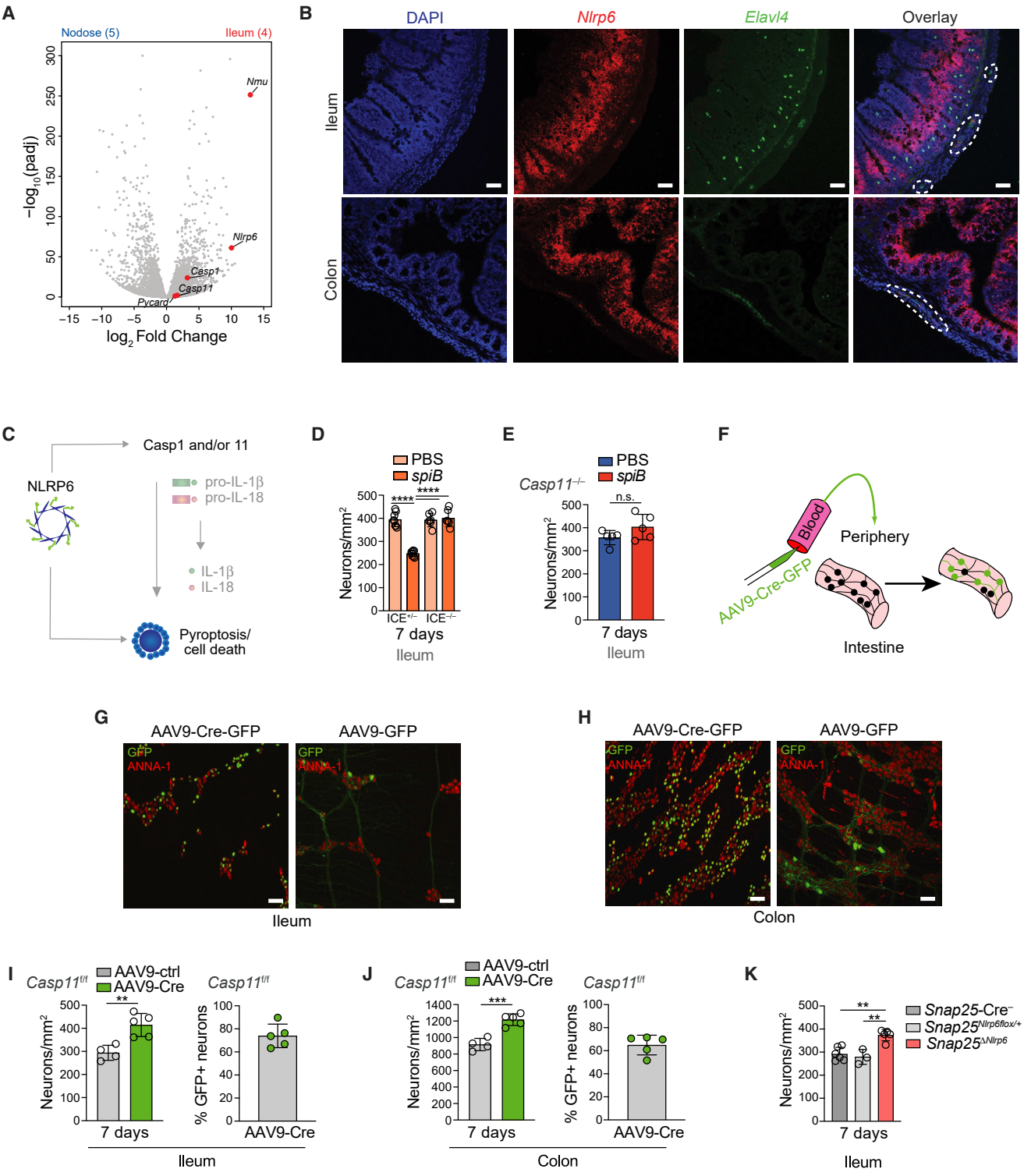

Figure 3. Infection-Induced iEAN Death Is Dependent on NLRP6 and Caspase 11 Expression

(A) Volcano plot of differentially expressed genes of TRAP-seq from neurons of the nodose ganglion (NG) and ileum myenteric iEANs isolated from *Snap25*^{RiboTag} mice. Grey dots highlight all genes analyzed; red dots highlight genes significantly differentially expressed in ileum iEANs. Number of samples are indicated in parentheses.

(legend continued on next page)

iEAN Loss Post-Enteric Infection Is *Nlrp6*- and *Casp11*-Dependent

To gain insights into a possible mechanism involved in infection-induced iEAN loss, we used neuronal-specific translating ribosomal affinity purification (TRAP) with *Snap25*^{RiboTag} mice, which allow neuronal-specific immunoprecipitation of actively translated mRNA (Muller et al., 2019). We compared iEANs with extrinsic neurons in the nodose ganglia (NG) of *Snap25*^{RiboTag} mice. Expression of HA-tagged ribosomes was confirmed in neurons of the myenteric plexus and NG of *Snap25*^{RiboTag} mice (Figure S3A). RNA sequencing analysis of immunoprecipitated intact mRNA bound to HA-tagged ribosomes (TRAP-seq) revealed iEAN-specific enrichment in genes encoding neuropeptides, such as neuromedin U (*Nmu*), as well as components of the inflammasome pathway (both canonical and non-canonical) including *Nlrp6*, *Pycard*, *Casp1*, and *Casp11* (Figure 3A). These data indicate that iEANs possess the machinery for engaging an inflammasome- and caspase 1 and/or 11 (Casp1 and/or 11)-mediated cell death. Imaging analyses for the expression of the inflammasome adaptor ASC (PYCARD) using an anti-ASC antibody in WT mice, or *Rosa26*$^{ASC:mCitrine}$ (ASC^{mCitrine}) reporter mice, confirmed the expression of this inflammasome component by iEANs of both naive and *spiB*-infected mice (Figures S3B and S3C). To visualize the *Nlrp6* expression pattern in iEANs, we performed fluorescence *in situ* hybridization (FISH) on ileum and colon sections using RNAscope probes specific to *Elavl4* (pan-neuronal) and *Nlrp6*. We observed dense localization of *Nlrp6* transcripts in the epithelium of the ileum and colon, similar to what has previously been reported (Levy et al., 2015). In addition, we visualized *Nlrp6* transcripts in areas of *Elavl4*-expressing cells in the *muscularis*, supporting the expression of *Nlrp6* by myenteric neurons (Figure 3B). Analysis of data from single-cell transcriptional profiling of iEANs (Zeisel et al., 2018) indicated that *Nlrp6* is highly enriched in excitatory iEANs compared with additional iEAN subsets (Figure S3D), providing an explanation for preferential loss of excitatory iEAN subsets during enteric infections.

To evaluate whether iEAN loss during infection is caspase-mediated, we first systemically administered a pan-caspase inhibitor (zVAD-FMK) to *spiB*-infected mice, which resulted in a reduction of iEAN loss (Figure S3E). We then directly addressed the role of caspases 1 and 11 in infection-induced iEAN loss by infecting Casp1 and 11 (ICE)-deficient or haplosufficient (ICE$^{+/-}$) mice with *spiB*. While ICE$^{+/-}$ mice exhibited pronounced iEAN loss 7 dpi, *spiB*-infected ICE$^{-/-}$ mice were completely protected from neuronal loss, despite similar bacterial clearance patterns (Figures 3C and 3D; Data S1). We further dissected the role of Casp1 and 11 separately by utilizing the 129S1/Sv mouse strain, which carries an inactivating mutation in the *Casp11* locus (human *Casp4*) (Kenneth et al., 2012). 129 mice infected with *spiB* exhibited no loss of colonic iEAN numbers as compared with non-infected controls (Figures S3F–S3J). This iEAN protection was independent of the ability of 129 mice to survive WT *Salmonella* infection because of expression of functional *Nramp* (Brown et al., 2013) because CBA/J mice, which also express a functional *Nramp* but do not carry a *Casp11* mutation, exhibited significant neuronal loss when infected with *spiB* despite similar clearance of the bacteria (Figures S3F–S3K) (data not shown). Furthermore, *spiB* infection did not result in iEAN loss in single *Casp11*-deficient mice (Figure 3E). These data suggest Casp11-mediated cell death as a main mechanism involved in iEAN loss following *Salmonella* infection.

To define whether the NLRP6 inflammasome and Casp11-mediated mechanisms proposed above are neuron intrinsic, we utilized two *in vivo* approaches of neuronal-specific gene deletion. Intravenous (i.v.) injection of AAV9 with neuronal-specific promoters can target iEANs, (Gombash et al., 2014), which we confirmed with i.v. administration of AAV9-hSyn-eGFP-Cre to *Rosa26*$^{lsl\text{-}tdTomato}$ reporter mice (Figure S3L). To remove *Casp11* from iEANs, we i.v.-injected *Casp11*$^{flox/flox}$ mice with AAV9-hSyn-eGFP-Cre or control AAV9-hSyn-eGFP viruses (Figures 3F–3H). We detected Cre-expressing AAV9 in 60%–90% of myenteric iEANs (Figures 3G–3J). Upon infection with *spiB,* we found no iEAN loss in mice injected with Cre-expressing AAV9 as compared with mice receiving the control virus (Figures 3I and 3J), suggesting that neuronal-intrinsic Casp11 expression is required for *Salmonella*-induced iEAN loss.

To address whether post-infectious iEAN loss is dependent on neuronal NLRP6, we crossed *Snap25*^{RiboTag} mice with *Nlrp6*-floxed (*Nlrp6*$^{flox/flox}$) mice (Figure S3M). We infected *Snap25*$^{\Delta Nlrp6}$, *Snap25*$^{RiboTagNlrp6flox/+}$ heterozygous, and (Cre−) *Nlrp6*$^{flox/flox}$ control mice with *spiB* and quantified iEAN numbers. While both heterozygous and Cre– controls showed reduced iEAN numbers upon *spiB* infection, *Snap25*$^{\Delta Nlrp6}$ did not display iEAN loss (Figure 3K). Together, the above data implicate neuronal-specific NLRP6 and Casp11 as main effectors of iEAN death following *Salmonella* infection.

(B) Fluorescence *in situ* hybridization RNAScope with probes for *Nlrp6* and *Elavl4* (pan-neuronal) in the ileum and colon from C57BL6/J mice. iEANs are outlined with a dashed line. Scale bars, 50 μm. Images representative of at least n = 2 per group.
(C) Scheme of the NLRP6 inflammasome pathway.
(D) Neuronal quantification as assessed by IF staining (ANNA-1) in the ileum myenteric plexus on day 7 post-gavage of PBS or *spiB* of *Casp1*$^{-/-}$ *Casp11*$^{-/-}$ (ICE$^{-/-}$) mice or heterozygous controls (ICE$^{+/-}$).
(E) Neuronal quantification (ANNA-1 staining) in the ileum myenteric plexus of *Casp11*$^{-/-}$ mice on day 7 post-*spiB* or -PBS gavage.
(F) Scheme of i.v. AAV9–mediated transduction of peripheral neurons.
(G and H) Representative confocal IF images of ileal (G) and colonic (H) myenteric plexus of *Casp11*$^{flox/flox}$ mice given i.v. injection of AAV9-hSyn-Cre-GFP or control viruses, stained with anti-ANNA-1 (red) antibodies. Scale bars, 50 μm. Images representative of at least n = 4 per condition.
(I and J) Left: neuronal quantification in the myenteric plexus of ileal (I) and colonic (J) segments from iEAN$^{\Delta Casp11}$ or *Casp11*$^{flox/flox}$ mice on day 7 post-*spiB* infection. Right: quantification of the number of Cre-GFP transduced cells in the ileum myenteric plexus of iEAN$^{\Delta Casp11}$ mice.
(K) Neuronal quantification in the ileum myenteric plexus from *Snap25*$^{Cre-}$, *Snap25*$^{Nlrp6flox/+}$, or *Snap25*$^{\Delta Nlrp6}$ mice on day 7 post-*spiB* infection.
Data are representative of 3–6 mice per condition. Data were analyzed by unpaired t test or ANOVA with Tukey's post-hoc test and are shown as mean ± SD; n.s. - not significant; **p ≤ 0.01, ***p ≤ 0.001, ****p ≤ 0.0001.
See also Figure S3 and Data S1.

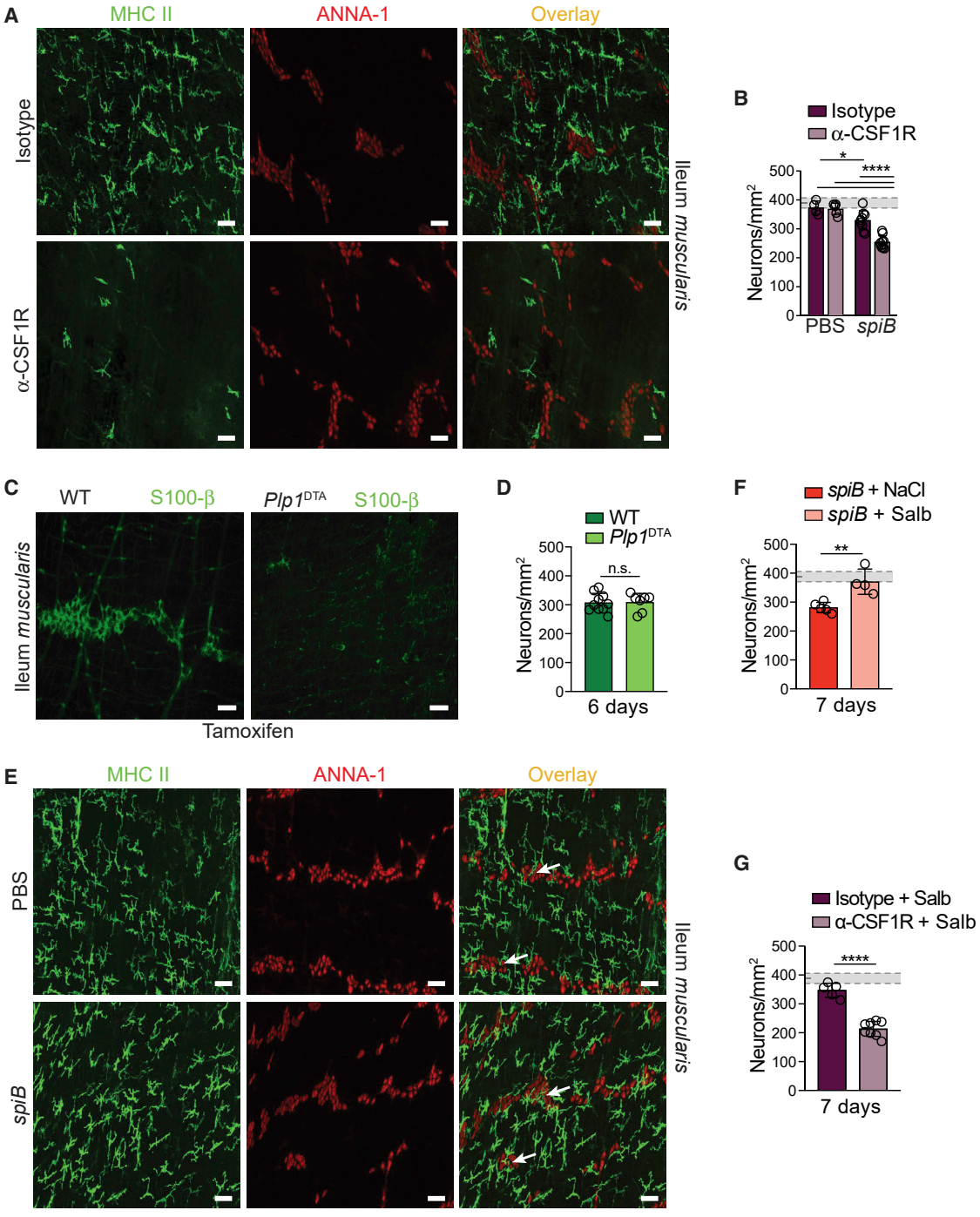

Figure 4. Tissue-Resident MMs Respond to Luminal Infection to Limit Neuronal Loss

(A and B) C57BL/6J mice were orally gavaged with PBS or *spiB* and treated with anti-CSF1R or IgG isotype control antibodies.

(A) Representative confocal IF staining of the ileum myenteric region stained with anti-MHC-II (green) and anti-ANNA-1 (red). Scale bars, 50 μm. Images representative of at least n = 5 per condition.

(B) Neuronal quantification of ileum myenteric plexus of injection-habituated non-infected and *spiB*-infected mice receiving anti-CSF1R or IgG isotype control.

(C) Representative confocal IF images of the ileum myenteric plexus of tamoxifen-treated *Plp1*^{iDTA} or control mice using anti-S100b (green). Samples obtained at 6 days post-gavage of *spiB*. Scale bars, 50 μm. Images representative of at least n = 5 per condition.

(D) Neuronal quantification of ileum myenteric plexus from *Plp1*^{iDTA} or control mice 6 days post-*spiB*.

(E) Representative confocal IF images from the ileum myenteric plexus of C57BL/6J mice using anti-MHC II (green) and anti-ANNA-1 (red). Samples obtained at 3 h post-gavage of PBS or *spiB*. Scale bars, 50 μm. Images representative of at least n = 5 per condition.

(legend continued on next page)

MMs Respond to Luminal Infection to Limit Neuronal Damage

Tissue-resident MMs, the most abundant immune cell population in the myenteric region, are closely juxtaposed to iEANs and have been linked to normal functioning of these neurons during homeostasis (De Schepper et al., 2018; Gabanyi et al., 2016; Muller et al., 2014). Our previous observations suggested that MMs possess a tissue-protective gene signature, including expression of *Retnla*, *Mrc1*, *Cd163*, and *Il10* at steady state (Gabanyi et al., 2016). To investigate a possible role of MMs in infection-induced iEAN loss, we first depleted MMs using an antibody-blocking colony-stimulating factor 1 receptor (CSF1R)-signaling, AFS98 (α-CSF1R), using a dose that preferentially depletes MMs over lamina propria macrophages (Muller et al., 2014) (Figures 4A, S4A, and S4B). Continuous α-CSF1R-mediated MM depletion did not impact iEAN numbers during steady state but resulted in an enhanced iEAN loss upon *spiB* infection compared with mice treated with the control antibody, despite similar bacterial load (Figure 4B; Data S1). These results indicate that, while short-term depletion of MMs does not impact iEAN survival in the unperturbed state, MMs may play an iEAN-protective role during enteric infection.

Glial cells, both in the CNS and periphery, have been reported to mediate neuronal protection (Brown et al., 2016). We thus evaluated their involvement in infection-induced iEAN loss or limiting thereof. To target enteric glia, we used mice carrying tamoxifen-inducible *Cre* under the glia-specific *Plp1* promotor (*Plp1*^{CreER}) and the *lox*-stop-*lox-DTA* transgene in the *Rosa26* locus (Rao et al., 2017). Depletion of glia in *Plp1*^{iDTA} mice before infection with *spiB* led to a similar loss of iEANs as tamoxifen-treated controls, indicating that enteric glia play neither a neuroprotective nor neurodetrimental role in this context (Figures 4C and 4D).

Next, we used confocal imaging to investigate MM dynamics upon early infection, which revealed a continuing presence and intercalation into ganglia of the myenteric plexus (Figures 4E and S4C). To assess whether inflammatory monocytes recruited from the circulation are involved in infection-induced neuronal damage, we used CCR2$^{-/-}$ mice, which exhibit an impairment in mobilizing inflammatory monocytes into tissues (Boring et al., 1997). CCR2$^{-/-}$ mice failed to clear *spiB* infection, likely reflecting reduced resistance in the mucosal layer (Dunay et al., 2008), and showed a mild acceleration rather than a delay in GITT (Figures S4D and S4E). Nonetheless, CCR2$^{-/-}$ mice showed similar iEAN loss as WT control mice (~25%), suggesting that the persistent luminal pathogen load does not cause an increase in neuronal damage (Figure S4F). These data highlight that intestinal macrophages recently differentiated from circulating monocyte precursors may contribute to *spiB* clearance mechanisms but are not required for post-infectious iEAN death. Together, the above results suggest a critical response of resident MMs to luminal pathogenic stimulation; while likely not essential for resistance mechanisms, they appear to prevent excessive neuronal damage.

β2-AR Signaling in MMs Constrains Infection-Induced Inflammation and Neuronal Death

We previously reported that the anti-inflammatory gene-expression profile of MMs was further enhanced following enteric infection via β_2-AR (Gabanyi et al., 2016). We investigated the capacity of β_2-AR signaling to mediate tissue protection by coupling pharmacological and genetic modulation of this pathway. First, we infected C57BL/6 mice with *spiB* while continuously administering a selective β_2-AR agonist (salbutamol) via osmotic pumps. While not affecting pathogen load, salbutamol treatment protected mice from iEAN loss (Figure 4F; Data S1). To directly assess the role of MMs in salbutamol-mediated neuroprotection, we depleted MM using α-CSF1R in mice receiving salbutamol. While we observed a rescue of iEAN death in mice treated with immunoglobulin G (IgG) isotype control antibody, MM depletion led to a loss of salbutamol-mediated iEAN protection (Figure 4G). Together, these data suggest that MMs are critical for β_2-AR-mediated iEAN protection.

We complemented these findings using a genetic approach by interbreeding mice carrying *Cre* recombinase under the myeloid *Lyz2* promoter (LysM^{Cre}) with *Adrb2*$^{flox/flox}$ mice (Hinoi et al., 2008). The specificity of Cre-targeting of macrophages in the intestinal *muscularis* was confirmed by IF and TRAP-seq analysis of LysM$^{\Delta Adrb2:\text{RiboTag}}$ and LysM$^{Adrbfl/:\text{RiboTag}}$ mice, which demonstrated macrophage-restricted HA expression, enrichment for macrophage-specific genes, and specific loss of *Adrb2* (Figures 5A–5C). Additionally, while we found occasional ectopic *Cre* expression in extrinsic ganglia, we were unable to detect iEAN recombination (Figure S5A). We did not detect infiltrating neutrophils, also targeted by *Lyz2*, in the intestinal *muscularis* at steady state or early post-infection, suggesting that neutrophil-β_2-AR signaling does not play a major role in this model (data not shown). Moreover, we found no differences in iEAN numbers or GITT in between LysM$^{\Delta Adrb2}$ and Cre− littermates during homeostasis (Figures S5B and S5C). LysM$^{\Delta Adrb2}$ and Cre− littermates exhibited similar *spiB* clearance upon infection (Figure 5D). However, LysM$^{\Delta Adrb2}$ mice had further increased fecal Lcn-2 levels post-infection, suggesting a role for myeloid-specific β_2-AR signaling in modulating infection-induced inflammation (Figure 5E). This was accompanied by prolonged GITT, which persisted long-term post-*spiB* clearance, an increased loss of iEANs, and enhanced alterations in ileal ring contractility (Figures 5F, 5G, and S5D). We then infected LysM$^{\Delta Adrb2}$ mice

(F) Neuronal quantification in the ileum myenteric plexus of C57BL/6J mice continuously receiving sodium chloride (NaCl) or salbutamol by osmotic pumps and orally gavaged PBS or *spiB* during drug treatment. Samples obtained on day 7 post-infection.

(G) Neuronal quantification in the ileum myenteric plexus of C57BL/6J mice receiving salbutamol delivered by subcutaneous osmotic pumps for 14 days. Mice were gavaged PBS or *spiB* on day 7 post-surgical pump implantation and received anti-CSF1R or IgG isotype control antibodies.

(B, F, and G) Shaded area indicates mean day 7 iEAN numbers ± SEM of all control C57BL6/J mice analyzed in Figure 1F.

Data are representative of at least n = 3 per condition. Data were analyzed by unpaired t test and are shown as mean ± SD; n.s. - not significant; *$p \leq 0.05$, **$p \leq 0.01$, ****$p \leq 0.0001$.

See also Figure S4 and Data S1.

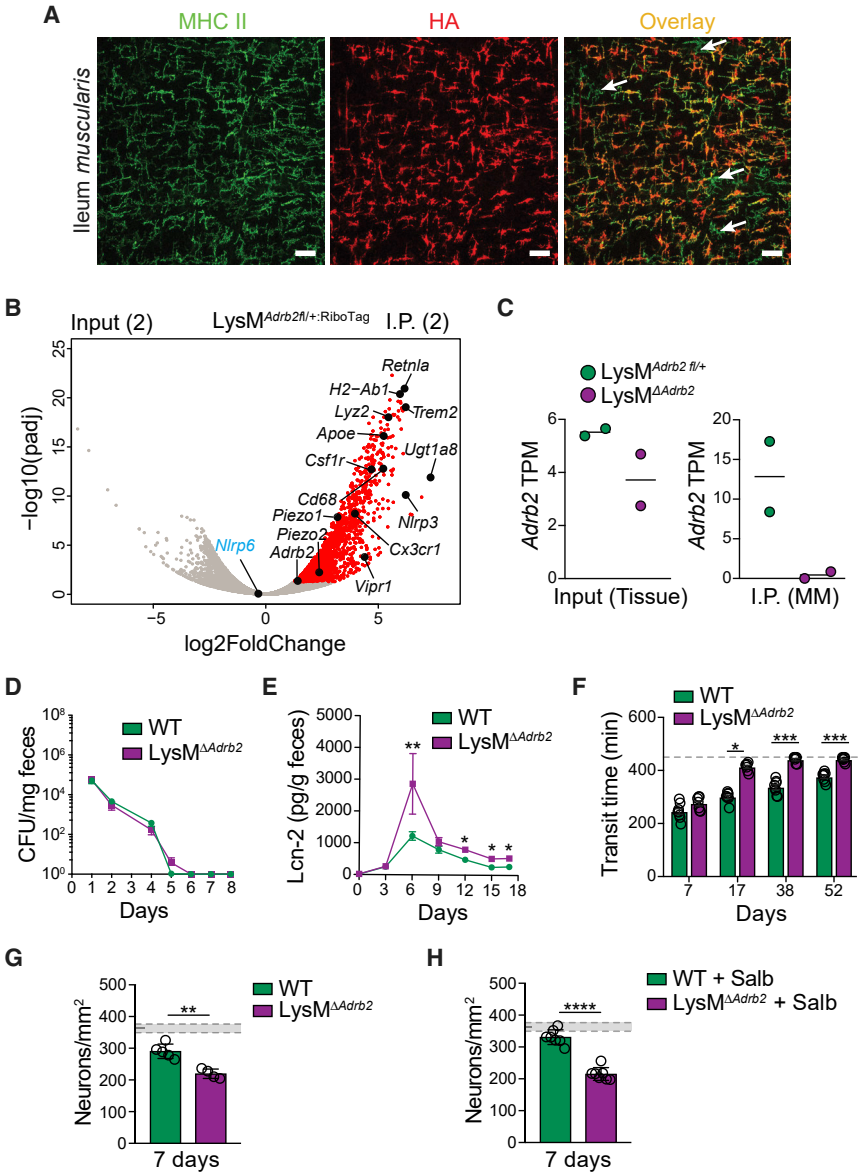

Figure 5. Loss of β_2-AR Signaling in MMs Exacerbates Neuronal Damage Following Enteric Infection

(A) IF staining of MMs from the ileum of LysM^{RiboTag} mice using anti-MHC II (green) and anti-HA (red) antibodies. White arrows indicate MHC II+ HA− macrophages. Scale bars, 50 μm. Images representative of n = 2 mice per group.

(B) Volcano plot of differential expression analysis (DEseq2) of TRAPseq from LysM$^{Adrb2fl/+:RiboTag}$ mice comparing input (ileum tissue) with immunoprecipitated (IP) transcripts (red dots) All IP samples indicated by red dots are log2FoldChange > 0.5 and padj > 0.05. Relevant macrophage genes highlighted in black text and *Nlrp6* (neuronal specific) highlighted in blue text.

(C) Transcripts per million (TPM) as calculated by Kallisto alignment of *Adrb2* transcript comparing input (ileum tissue) or IP transcripts from LysM$^{Adrb2fl/+:RiboTag}$ and LysM$^{\Delta Adrb2:RiboTag}$ mice.

(D–H) LysM$^{\Delta Adrb2}$ and WT littermate control mice were orally infected with *spiB*.

(D) Quantification of fecal CFU on the indicated days post-infection.

(E) Quantification of fecal lipocalin-2 (Lcn-2) on the indicated days post-infection.

(F) Total GI transit time; experiments were ended at 450 min (dashed line).

(G and H) Neuronal quantification in the ileum myenteric plexus on day 7 post-*spiB* infection of LysM$^{\Delta Adrb2}$ mice and WT littermates (G), shaded area indicates mean day 7 iEAN numbers ± SEM of non-infected LysM$^{\Delta Adrb2}$ mice and WT littermates (Figure S5B); LysM$^{\Delta Adrb2}$ and WT littermates receiving salbutamol via subcutaneous osmotic pumps and infected with *spiB* post-implantation (H), shaded area indicates mean day 7 iEAN numbers ± SEM of non-infected LysM$^{\Delta Adrb2}$ and WT littermate mice (Figure S5B).

Unless indicated otherwise, data are representative of 3–6 mice per condition, were analyzed by unpaired t test or ANOVA with Tukey's post-hoc test, and are shown as mean ± SD; *p ≤ 0.05, **p ≤ 0.01, ***p ≤ 0.001, ****p ≤ 0.0001.

See also Figure S5 and Data S1.

and Cre− littermates receiving continuous salbutamol treatment, which resulted in prevention of iEAN loss in Cre− littermates carrying intact myeloid β_2-AR. However, this neuroprotection was absent in salbutamol-treated LysM$^{\Delta Adrb2}$ mice (Figure 5H). These data establish a role for β_2-AR signaling in intestinal macrophages that contributes to a neuroprotective program following enteric infection.

Local Sympathetic Activation Mediates iEAN Protection during Enteric Infection

We noted that mice intraperitoneally (i.p.)-injected multiple times with IgG isotype antibody (as in MM-depletion experiments) or mice anesthetized with isoflurane (as in control pump experiments) did not lose usual ~25% iEAN numbers post-*spiB* infection, suggesting that stress-induced local or systemic catecholamine release could trigger the same protective pathway in MMs. Indeed, a short pulse of isoflurane anesthesia or i.p. injections of PBS or IgG isotype antibody were sufficient to prevent iEAN death following *spiB* infection, indicating that stress signals able to potentiate β_2-AR signaling may help prevent post-infectious iEAN loss (Figures S6A and S6B). In light of these findings, we sought to determine whether systemic release of catecholamines from the hypothalamic-pituitary-adrenal axis could play a role in neuronal protection during infection. We performed bilateral adrenalectomy on WT mice and compared iEAN loss upon *spiB* infection with sham-operated controls. Rather than enhanced iEAN loss observed in LysM$^{\Delta Adrb2}$ mice, adrenalectomized animals showed reduced neuronal loss, suggesting that systemic catecholamines were not required for iEAN protection and, furthermore, that additional stress hormones produced by

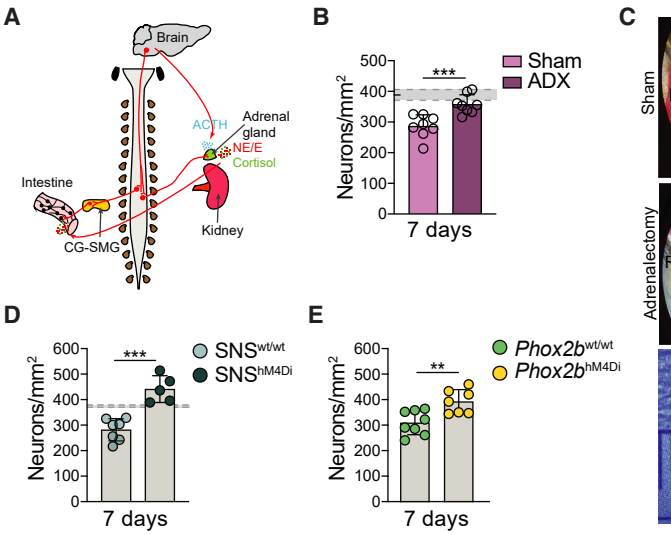

Figure 6. Activation of Gut Sympathetic Neurons Protects iEAN Death Following Enteric Infection

(A) Scheme of hypothalamic-pituitary-adrenal (HPA) axis and local sympathetic innervation of the intestine.

(B, D, and E) Mice were orally infected with *spiB*. Neuronal quantification in the ileum myenteric plexus on day 7 post-*spiB* infection.

(B) Adrenalectomized (ADX) or sham-operated C57BL/6J mice.

(C) Images demonstrating successful removal of adrenal glands from C57BL/6J mice.

(D and E) SNS^{hM4Di} (D) or *Phox2b*^{hM4Di} (E) mice were treated with 10 mg/kg Compound 21 (C21) 24 h before *spiB* infection.

Abbreviations are as follows: NE, norepinephrine (noradrenaline); E, epinephrine (adrenaline); CG-SMG, celiac-superior mesenteric ganglion. Data are representative of at least n = 3 per condition. Data were analyzed by unpaired t test and are shown as mean ± SD; $^{**}p \leq 0.01$, $^{***}p \leq 0.001$. See also Figure S6 and Data S1.

the adrenal glands (corticosteroids) could play a detrimental role in enteric neuronal survival during intestinal infections (Figures 6A–6C).

We previously demonstrated that *spiB* infection led to a significant increase in the number of recently activated, cFos+ sympathetic neurons in the celiac-superior mesenteric ganglion (CG-SMG) (Gabanyi et al., 2016). We thus assessed whether stimulation of these neurons is sufficient to drive MM-β_2-AR-mediated tissue protection. We utilized two chemogenetic mouse models in which administration of the synthetic ligand Compound 21 to mice carrying an inactivating designer receptor exclusively activated by designer drugs (DREADD) driven by promoters that are active in sensory nodose ganglia neurons (SNS^{hM4Di} or *Phox2b*^{hM4Di}) results in a significant increase in cFos expression by gut-projecting sympathetic neurons (Muller et al., 2019). We found that DREADD-induced activation of gut-projecting neurons prior to *spiB* infection both in SNS^{hM4Di} and *Phox2b*^{hM4Di} mice significantly rescued iEAN loss (Figures 6D and 6E). These results provide further support of a role for locally released catecholamines and β_2-AR signaling in MMs in limiting inflammation-induced iEAN loss.

An Adrenergic-Arginase 1-Polyamine Axis in MM Limits Infection-Induced Neuronal Loss

To dissect possible mechanisms in which MM β_2-AR signaling is involved in preventing excessive tissue damage post-infection, we analyzed LysM$^{\Delta Adrb2}$ MM gene expression profiles. MMs sorted from Cre− littermates responded to *spiB* infection by upregulating tissue-protective genes upon infection, but we did not observe this upregulation in MMs sorted from infected LysM$^{\Delta Adrb2}$ mice (Figure 7A). Arginase 1 (Arg1) is known to mediate the production of neuroprotective polyamines such as spermine (Cai et al., 2002), which in turn was described to suppress NLRP6-inflammasome activation (Levy et al., 2015). To investigate the participation of polyamines in iEAN cell death, we supplemented the drinking water of *spiB*-infected mice with spermine or with difluoromethylornithine (DFMO), which inhibits polyamine biosynthesis by selective and irreversible inhibition of ornithine decarboxylase 1 (ODC1) (Koomoa et al., 2013). Bacterial load and clearance patterns were similar in either treatment condition; however, mice that received DFMO exhibited enhanced iEAN loss, while those receiving spermine showed a significant rescue post-*spiB* infection (Figures 7B and 7C; Data S1). Finally, we genetically addressed whether Arg1 activity in MMs was required for their protective role in infection-induced neuronal damage in the intestine by interbreeding LysM^{Cre} and *Arg1*$^{flox/flox}$ mice (El Kasmi et al., 2008). We did not observe differences in iEAN numbers in LysM$^{\Delta Arg1}$ mice compared with Cre− controls during homeostasis (Figure S7A). Upon *spiB* infection, LysM$^{\Delta Arg1}$ also showed similar pathogen load and clearance patterns but a trend to increased GITT (Figure S7B; Data S1). However, loss of myeloid Arg1 heightened iEAN loss post-*spiB* infection (Figure 7D). Together, these results point to a functional role for a MM β_2-AR-Arg1-polyamine axis in in limiting infection-induced enteric neuronal cell death.

DISCUSSION

Inflammation-Induced Neuronal Damage

Overt inflammation in response to infection can result in chronic immunopathology. In the GI tract, bacterial, viral, and protozoan infections are associated with intestinal neuropathy and the development of post-infectious IBS (Beatty et al., 2014; Holschneider et al., 2011; Ohman and Simrén, 2010; White et al., 2018). However, the understanding of underlying mechanisms involved in this process is largely lacking. Here, we provide evidence that MMs located in close proximity to enteric neurons prevent infection- or inflammation-induced tissue damage, perhaps an analogous function to that described for microglia in the CNS (Davalos et al., 2005; Wang et al., 2015).

Most mechanisms proposed for inflammation-induced neuronal damage thus far are related to CNS neuroinflammation. The apparent link observed in our study, between having a "normal" microbiota and iEAN recovery, offers an interesting

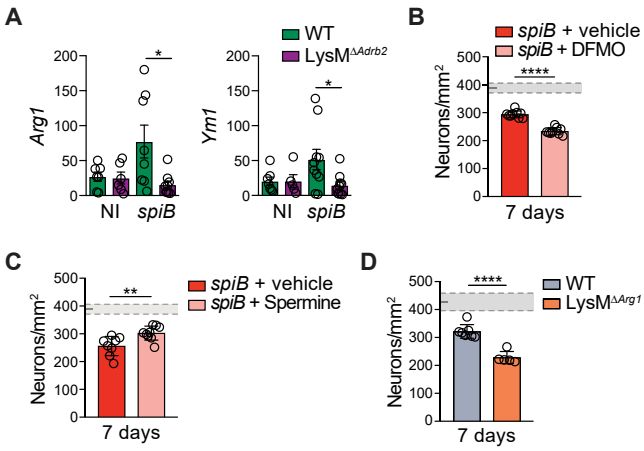

Figure 7. An Adrenergic-Arginase 1-Polyamine Axis in MMs Limits Infection-Induced Neuronal Death

(A) mRNA expression analysis of the indicated genes by quantitative real-time PCR in LysM$^{\Delta Adrb2}$ and WT littermate control mice non-infected (NI) or 2 h post-infection with *spiB*.

(B–D) Neuronal quantification in the ileum myenteric plexus on day 7 post-infection with *spiB* of (B) C57BL/6J mice with access to regular drinking water or water supplemented with DFMO over the course of infection, shaded area indicates mean day 7 iEAN numbers ± SEM of all control C57BL6/J mice (Figure 1F); (C) C57BL/6J mice receiving regular drinking water or water supplemented with spermine over the course of infection, shaded area bounded by dashed lines indicates mean day 7 iEAN numbers ± SEM of all control C57BL6/J mice; (D) LysM$^{\Delta Arg1}$ mice and WT littermates, shaded area indicates mean day 7 iEAN numbers ± SEM of non-infected LysM$^{\Delta Arg1}$ and WT littermate control mice (Figure S7A).

Data are representative of 3–6 mice per condition. Data were analyzed by unpaired t test or ANOVA with Bonferroni correction and are shown as mean ± SD; *p ≤ 0.05, **p ≤ 0.01, ****p ≤ 0.0001.

See also Figure S7 and Data S1.

direction for studies of central and peripheral neuropathies. For instance, what are the mechanisms utilized by the gut microbiota to maintain, or rescue, neuronal populations? Do specific bacterial species play a beneficial or detrimental role in this process? Although certain inflammatory processes are essential for neuronal function and tissue physiology, including neuronal pruning and tissue repair (Salter and Stevens, 2017), excessive inflammation often results in the production of neurotoxic factors such as interleukin 1 beta (IL-1β) and tumor necrosis factor alpha (Crotti and Glass, 2015). While some of these could play a role in enteric infections, our studies rather point to NLRP6 ligands, or alternative triggers of Casp11 cleavage, as mediators of infection-induced iEAN cell death. These results corroborate previous work describing a protective phenotype in *Pycard*$^{-/-}$ mice that did not lose enteric neurons following DNBS-induced colitis, a process that was shown not to involve the NLPR3 inflammasome (Gulbransen et al., 2012). Unlike the indiscriminate iEAN loss previously observed in chemically induced murine colitis models (Mawe, 2015), our studies indicate infection-induced location- and subset-specific loss of excitatory iEANs. These data warrant further study and additional subset-specific analysis of EANs in the steady state or under pathological conditions. Nevertheless, we speculate that enteric neuronal utilization of components of the NLRP6 inflammasome machinery and downstream effectors, put forward here in the context of neuronal loss post-enteric infection, may be engaged in other contexts. For instance, as demonstrated in this issue of *Cell*, iEAN-mediated production of IL-18 can participate in pathogen resistance mechanisms (Jarret et al., 2020). Additionally, heterologous infection experiments suggest the existence of either a form of tissue memory (trained immunity) or a limited subset of enteric neurons expressing such inflammasome machinery—possibilities that warrant further investigation. Furthermore, it remains to be determined whether neurodegenerative processes in the CNS also involve this or analogous pathways (Song and Colonna, 2018).

Monocyte-Macrophage Lineage and Enteric Glia in Neuronal Damage

Previous studies have uncovered a potential role of monocytes, macrophages, and microglia in the induction or modulation of inflammation-induced neuropathy, CNS damage, and subsequent changes in animal behavior (Aguzzi et al., 2013; D'Mello et al., 2013). Tissue-resident macrophage populations in the brain express pattern-recognition receptors (PRRs) and are believed to contribute significantly to dendritic spine remodeling (Parkhurst et al., 2013; Song and Colonna, 2018). The balance between the production of pro-inflammatory and tissue-protective factors by macrophage populations is likely to determine the pathological versus reparative role of these cells. In a model mimicking CNS virus infection, depletion of monocytes abrogated dendritic spine loss (Parkhurst et al., 2013), indicating that in the CNS, multiple cell types can mediate similar effects. In the gut, lack of inflammatory monocytes failed to impact iEAN loss, suggesting a dependence on longer-lived resident macrophage populations, whose presence in the gut were only recently proposed (De Schepper et al., 2018; Shaw et al., 2018). Under conditions of stress or inflammation, activation of enteric glia has also been linked to neuronal damage (Brown et al., 2016; Gulbransen et al., 2012; Mayo et al., 2014), yet little is known about the relevance of glial-immune cell interactions in the GI tract. While our experiments depleting enteric glia did not suggest a major role in the infection-induced iEAN loss, it remains plausible that surrounding enteric glia, or MMs, induce neuronal damage in other contexts that were previously attributed to microglia in the brain (Jin et al., 2016).

Both glial cells and tissue macrophages are also appreciated to prevent inflammation-induced damage in several contexts, as well as to initiate repair processes post-injury. In models of spinal cord injury, incoming monocytes are thought to mediate a functional recovery via secretion of anti-inflammatory mediators (Shechter et al., 2009), although an enhancement of inflammatory markers in macrophages was also shown to help CNS axonal regeneration (Gensel et al., 2009). Our data favor a neuroprotective role for MMs via upregulation of Arg1 and polyamine production, an analogous observation to previous studies suggesting that "alternatively activated" macrophages promote axonal growth or regeneration after CNS injury (Cai et al., 2002; Kigerl et al., 2009). While multiple studies of the CNS find a direct role for polyamines in neuro-regeneration (Mahar and Cavalli, 2018), our data suggest a potential role for these molecules in preventing neuronal cell death modulation of the inflammasome. This possibility is supported by previous studies

demonstrating that microbiota-derived spermine regulates NLRP6 signaling and intestinal epithelial cell secretion of IL-18 (Levy et al., 2015), which could also play tissue-protective roles in the enteric infection models described here. Nonetheless, macrophages differentiated toward an ''alternatively activated'' phenotype could also negatively contribute to gut homeostasis during the resolution of inflammatory processes, for instance, by enhancing fibrosis (Xue et al., 2015). Finally, because we previously demonstrated that macrophages located in the mucosal layer do not show an immediate upregulation of tissue-protective genes upon enteric infection, an anatomically segregated model in which lamina propria macrophages help pathogen resistance and MMs boost tolerance is conceivable.

Sensing and Regulation of the Catecholamine-β_2-AR Pathway

The nervous and immune systems are the body's main sensory interfaces, and both depend on cell-to-cell contacts and on soluble molecules that act on proximal or distant target cells, which include neurons and immune cells themselves (Besedovsky et al., 1983). The involvement of catecholaminergic neurons in anti-inflammatory responses has been demonstrated in different tissues and is attributed to the broad sympathetic innervation in peripheral lymph nodes associated with expression of β_2-AR in immune cells (Pavlov et al., 2018). Our findings also suggest an intricate interplay between iEANs, macrophages, and eEANs (extrinsic enteric-associated neurons), particularly the extrinsic sympathetic ganglia, adding functional significance to observations of interactions between barrier tissue-resident macrophages and peripheral neurons (Gabanyi et al., 2016; Muller et al., 2014). The source of catecholamines may be context dependent: enteric infections may result in the activation of extrinsic sympathetic neurons (Gabanyi et al., 2016); under conditions of systemic stress, these signals could originate from the adrenal glands, although our adrenalectomy experiments argue against this possibility. The effects of stress are typically thought to be immunosuppressive; however, in the context of cellular damage and death, glucocorticoids can promote pro-inflammatory immune responses, particularly in the CNS (Di Giovangiulio et al., 2015; Salgo et al., 2006). We found that acute stress in mice provided significant protection to iEANs during enteric infection, results that more broadly link physiological stress to control of inflammation. In light of these findings, stress should be considered as a confounding factor to control for in the context of inflammation. Nevertheless, both of these pathways require neural input, yet the circuitry connecting luminal sensing to eEAN activation (and a possible involvement of the CNS), and how luminal stimulations can regulate it, remain to be determined (Muller et al., 2019; Prüss et al., 2017). Current literature suggests that sensing of luminal pathogens, or associated changes in the microenvironment, could be mediated by enteroendocrine cells (Kaelberer et al., 2018) or epithelial and mucosal-associated sensory afferents (Chiu et al., 2013), both with the capacity to impact iEAN survival or initiate changes in eEAN activity. However, the components of luminal sensing still require further dissection to uncover relevant cell populations and receptors (Veiga-Fernandes and Mucida, 2016). Downstream of the initial components, our data identify a novel mechanism of neuronal cell death and point to a role for tissue-resident MMs in limiting neuronal damage. Such intra-tissue adaptation of immune cells appears to help the maintenance of a proper balance between resistance and tolerance, and these findings could have implications in additional tissues and contexts.

STAR★METHODS

Detailed methods are provided in the online version of this paper and include the following:

- KEY RESOURCES TABLE
- LEAD CONTACT AND MATERIALS AVAILABILITY
- EXPERIMENTAL MODEL AND SUBJECT DETAILS
  - Mice
  - Microorganisms
- METHOD DETAILS
  - Infections
  - Antibodies and flow cytometry
  - Intestine dissection
  - Nodose ganglion dissection
  - Intestine motility measurements
  - Ileal smooth muscle contractility
  - Lipocalin-2 ELISA
  - Drug Administration
  - Isoflurane induction
  - Sham intraperitoneal injections
  - Subcutaneous pump implantation
  - Adrenalectomy
  - Generation of *Nlrp6*$^{flox/flox}$ mice
  - 16S sample processing
  - 16S sequencing
  - Chemogenetics
  - Antibiotic-mediated microbiota depletion and re-colonization
  - Anti-CSF1R (ASF98) antibody production
  - MM depletion using anti-CSF1R
  - Immunocytochemistry
  - Whole-mount intestine immunofluorescence
  - Confocal imaging
  - RiboTag
  - RNA-sequencing
  - Mining of published iEAN scRNA-seq
  - Cryosectioning of fresh-frozen tissue
  - RNA fluorescence *in situ* hybridization (FISH) using RNAscope® technology
  - Neuronal quantification
  - Macrophage intercalation calculation
  - 3D image reconstruction for MM ganglionic intercalation calculations
  - Colony forming unit counting
  - Determination of caspase 11 mutation status by PCR and Sanger Sequencing
  - Single Cell Suspension of Intestinal Macrophages
  - Quantitative PCR
  - AAV9 Transduction of iEAN
  - Induction of glia depletion
- QUANTIFICATION AND STATISTICAL ANALYSIS
  - Statistical analysis

- DATA AND CODE AVAILABILITY
  - Data resources
  - Code resources

SUPPLEMENTAL INFORMATION

Supplemental Information can be found online at https://doi.org/10.1016/j.cell.2019.12.002.

ACKNOWLEDGMENTS

We thank all Mucida Lab members, past and present, for their help; G. Victora (Rockefeller University [RU]) and J. Lafaille (New York University) and their lab members for helpful discussions; A. Rogoz and S. Gonzales (RU) for maintenance and genotyping of mice; T. Catarino (Champalimaud Center for the Unknown) for help with EAN quantification; A. North and the RU Bio-imaging Research Center for assistance with image acquisition analysis; the RU Genomics Center for RNA sequencing; and the RU employees for continuous assistance. We thank S. Ackerman, P. Cohen (RU), and P. Woster (Medical University of South Carolina) for providing DFMO and expertise; Vanda A. Lennon (The Mayo Clinic) for generously sharing anti-ANNA-1; R. Gazzinelli (University of Massachusetts) for *T. cruzi* and *T. gondii* strains; and I. Brodsky (University of Pennsylvania) for kindly providing *Y. pseudotuberculosis* and protocols. We also thank S. Galli and K. Matsushita (Stanford University) for providing *S. venezuelensis* and expertise; M. Merad (MSSM) for kindly sharing the ASF98 hybridoma cell line; P. Frenette (Albert Einstein College of Medicine) and G. Enikolopov (Stony Brook University) for *Nestin*^{GFP} mice; G. Karsenty (Columbia University Medical Center) and A. Wullaert (Ghent University) for generously providing Adrb2$^{flox/flox}$ and Casp11$^{flox/flox}$ mice, respectively; and T. Kanneganti (St. Jude Children's Research Hospital) the NLRP6$^{flox/flox}$ strain. This work was supported by a National Institutes of Health (NIH) F31 Kirchstein Fellowship (to P.A.M.), National Center for Advancing Translational Sciences NIH UL1TR001866 (to P.A.M. and D.M.), an Anderson Graduate Fellowship (to F.M.), The Rockefeller University Women in Science Fellowship (to F.M.), a Philip M. Levine Fellowship (to P.A.M.), a Kavli Graduate Fellowship (to P.A.M.), the Leona M. and Harry B. Helmsley Charitable Trust (to F.M., P.A.M., C.L.G., and D.M.), the Human Frontier Science Program (to T.A.), the Excellence Cluster 2167 Precision Medicine in Inflammation and the German Research Foundation CRC1182 (to P.R.), the Crohn's & Colitis Foundation of America (to D.M.), the Kenneth Rainin Foundation (to D.M.), and NIH grants R01 DK093674 and R01 DK113375 (to D.M.).

AUTHOR CONTRIBUTIONS

Conceptualization, P.A.M. and D.M.; Methodology, F.M., P.A.M., C.L.G, and I.G.; Software, P.A.M.; Validation, F.M., P.A.M., C.L.G., I.G., Z.J.K., D.C.-B., and T.A.; Formal Analysis, F.M., P.A.M., C.L.G., I.G., Z.J.K., and D.C.-B.; Investigation, F.M., P.A.M., C.L.G., I.G., Z.J.K., D.C.-B., and T.A.; Resources, P.R.; Data Curation, F.M. and P.A.M.; Writing – Original Draft, F.M., P.A.M., C.L.G., and D.M.; Writing – Review & Editing, F.M., P.A.M., C.L.G., I.G., and D.M.; Visualization, F.M., C.L.G., P.A.M., I.G., Z.J.K., D.C.-B., and T.A.; Supervision, D.M. and P.A.M.; Project Administration, P.A.M and D.M.; Funding Acquisition, P.A.M. and D.M.

DECLARATION OF INTERESTS

The authors declare no competing interests.

Received: February 20, 2019
Revised: September 25, 2019
Accepted: December 3, 2019
Published: January 9, 2020

REFERENCES

Aguzzi, A., Barres, B.A., and Bennett, M.L. (2013). Microglia: scapegoat, saboteur, or something else? Science *339*, 156–161.

Arantes, R.M., Marche, H.H., Bahia, M.T., Cunha, F.Q., Rossi, M.A., and Silva, J.S. (2004). Interferon-gamma-induced nitric oxide causes intrinsic intestinal denervation in Trypanosoma cruzi-infected mice. Am. J. Pathol. *164*, 1361–1368.

Balemans, D., Mondelaers, S.U., Cibert-Goton, V., Stakenborg, N., Aguilera-Lizarraga, J., Dooley, J., Liston, A., Bulmer, D.C., Vanden Berghe, P., Boeckxstaens, G.E., and Wouters, M.M. (2017). Evidence for long-term sensitization of the bowel in patients with post-infectious-IBS. Sci. Rep. *7*, 13606.

Beatty, J.K., Bhargava, A., and Buret, A.G. (2014). Post-infectious irritable bowel syndrome: mechanistic insights into chronic disturbances following enteric infection. World J. Gastroenterol. *20*, 3976–3985.

Besedovsky, H., del Rey, A., Sorkin, E., Da Prada, M., Burri, R., and Honegger, C. (1983). The immune response evokes changes in brain noradrenergic neurons. Science *221*, 564–566.

Boring, L., Gosling, J., Chensue, S.W., Kunkel, S.L., Farese, R.V., Jr., Broxmeyer, H.E., and Charo, I.F. (1997). Impaired monocyte migration and reduced type 1 (Th1) cytokine responses in C-C chemokine receptor 2 knockout mice. J. Clin. Invest. *100*, 2552–2561.

Bray, N.L., Pimentel, H., Melsted, P., and Pachter, L. (2016). Near-optimal probabilistic RNA-seq quantification. Nat Biotechnol. *34*, 525–527.

Brown, D.E., Libby, S.J., Moreland, S.M., McCoy, M.W., Brabb, T., Stepanek, A., Fang, F.C., and Detweiler, C.S. (2013). Salmonella enterica causes more severe inflammatory disease in C57/BL6 Nramp1G169 mice than Sv129S6 mice. Vet. Pathol. *50*, 867–876.

Brown, I.A., McClain, J.L., Watson, R.E., Patel, B.A., and Gulbransen, B.D. (2016). Enteric glia mediate neuron death in colitis through purinergic pathways that require connexin-43 and nitric oxide. Cell. Mol. Gastroenterol. Hepatol. *2*, 77–91.

Cai, D., Deng, K., Mellado, W., Lee, J., Ratan, R.R., and Filbin, M.T. (2002). Arginase I and polyamines act downstream from cyclic AMP in overcoming inhibition of axonal growth MAG and myelin in vitro. Neuron *35*, 711–719.

Chiu, I.M., Heesters, B.A., Ghasemlou, N., Von Hehn, C.A., Zhao, F., Tran, J., Wainger, B., Strominger, A., Muralidharan, S., Horswill, A.R., et al. (2013). Bacteria activate sensory neurons that modulate pain and inflammation. Nature *501*, 52–57.

Crotti, A., and Glass, C.K. (2015). The choreography of neuroinflammation in Huntington's disease. Trends Immunol. *36*, 364–373.

D'Mello, C., Riazi, K., Le, T., Stevens, K.M., Wang, A., McKay, D.M., Pittman, Q.J., and Swain, M.G. (2013). P-selectin-mediated monocyte-cerebral endothelium adhesive interactions link peripheral organ inflammation to sickness behaviors. J. Neurosci. *33*, 14878–14888.

Davalos, D., Grutzendler, J., Yang, G., Kim, J.V., Zuo, Y., Jung, S., Littman, D.R., Dustin, M.L., and Gan, W.B. (2005). ATP mediates rapid microglial response to local brain injury in vivo. Nat. Neurosci. *8*, 752–758.

De Schepper, S., Verheijden, S., Aguilera-Lizarraga, J., Viola, M.F., Boesmans, W., Stakenborg, N., Voytyuk, I., Smidt, I., Boeckx, B., Dierckx de Casterle, I., et al. (2018). Self-Maintaining Gut Macrophages Are Essential for Intestinal Homeostasis. Cell *175*, 400–415 e413.

Di Giovangiulio, M., Verheijden, S., Bosmans, G., Stakenborg, N., Boeckxstaens, G.E., and Matteoli, G. (2015). The Neuromodulation of the Intestinal Immune System and Its Relevance in Inflammatory Bowel Disease. Front. Immunol. *6*, 590.

Dunay, I.R., Damatta, R.A., Fux, B., Presti, R., Greco, S., Colonna, M., and Sibley, L.D. (2008). Gr1(+) inflammatory monocytes are required for mucosal resistance to the pathogen Toxoplasma gondii. Immunity *29*, 306–317.

Dutra, W.O., Menezes, C.A., Villani, F.N., da Costa, G.C., da Silveira, A.B., Reis, Dd., and Gollob, K.J. (2009). Cellular and genetic mechanisms involved in the generation of protective and pathogenic immune responses in human Chagas disease. Mem. Inst. Oswaldo Cruz *104* (*Suppl 1*), 208–218.

Edgar, R.C. (2010). Search and clustering orders of magnitude faster than BLAST. Bioinformatics *26*, 2460–2461.

El Kasmi, K.C., Qualls, J.E., Pesce, J.T., Smith, A.M., Thompson, R.W., Henao-Tamayo, M., Basaraba, R.J., König, T., Schleicher, U., Koo, M.S., et al. (2008). Toll-like receptor-induced arginase 1 in macrophages thwarts effective immunity against intracellular pathogens. Nat. Immunol. *9*, 1399–1406.

Esterházy, D., Canesso, M.C.C., Mesin, L., Muller, P.A., de Castro, T.B.R., Lockhart, A., ElJalby, M., Faria, A.M.C., and Mucida, D. (2019). Compartmentalized gut lymph node drainage dictates adaptive immune responses. Nature *569*, 126–130.

Fonseca, D.M., Hand, T.W., Han, S.J., Gerner, M.Y., Glatman Zaretsky, A., Byrd, A.L., Harrison, O.J., Ortiz, A.M., Quinones, M., Trinchieri, G., et al. (2015). Microbiota-Dependent Sequelae of Acute Infection Compromise Tissue-Specific Immunity. Cell *163*, 354–366.

Furness, J.B., Rivera, L.R., Cho, H.J., Bravo, D.M., and Callaghan, B. (2013). The gut as a sensory organ. Nat. Rev. Gastroenterol. Hepatol. *10*, 729–740.

Gabanyi, I., Muller, P.A., Feighery, L., Oliveira, T.Y., Costa-Pinto, F.A., and Mucida, D. (2016). Neuro-immune Interactions Drive Tissue Programming in Intestinal Macrophages. Cell *164*, 378–391.

Gensel, J.C., Nakamura, S., Guan, Z., van Rooijen, N., Ankeny, D.P., and Popovich, P.G. (2009). Macrophages promote axon regeneration with concurrent neurotoxicity. J. Neurosci. *29*, 3956–3968.

Gombash, S.E., Cowley, C.J., Fitzgerald, J.A., Hall, J.C., Mueller, C., Christofi, F.L., and Foust, K.D. (2014). Intravenous AAV9 efficiently transduces myenteric neurons in neonate and juvenile mice. Front. Mol. Neurosci. *7*, 81.

Gulbransen, B.D., Bashashati, M., Hirota, S.A., Gui, X., Roberts, J.A., MacDonald, J.A., Muruve, D.A., McKay, D.M., Beck, P.L., Mawe, G.M., et al. (2012). Activation of neuronal P2X7 receptor-pannexin-1 mediates death of enteric neurons during colitis. Nat. Med. *18*, 600–604.

Hinoi, E., Gao, N., Jung, D.Y., Yadav, V., Yoshizawa, T., Myers, M.G., Jr., Chua, S.C., Jr., Kim, J.K., Kaestner, K.H., and Karsenty, G. (2008). The sympathetic tone mediates leptin's inhibition of insulin secretion by modulating osteocalcin bioactivity. J. Cell Biol. *183*, 1235–1242.

Holschneider, D.P., Bradesi, S., and Mayer, E.A. (2011). The role of experimental models in developing new treatments for irritable bowel syndrome. Expert Rev. Gastroenterol. Hepatol. *5*, 43–57.

Holst, M.C., and Powley, T.L. (1995). Cuprolinic blue (quinolinic phthalocyanine) counterstaining of enteric neurons for peroxidase immunocytochemistry. J. Neurosci. Methods *62*, 121–127.

Jarret, A., Jackson, R., Duizer, C., Healy, M.E., Zhao, J., Rone, J.M., Bielecki, P., Sefik, E., Roulis, M., Rice, T., et al. (2020). Enteric Nervous System-Derived IL-18 Orchestrates Mucosal Barrier Immunity. Cell *180*. Published online January 9, 2020. https://doi.org/10.1016/j.cell.2019.11.014.

Jin, S., Kim, J.G., Park, J.W., Koch, M., Horvath, T.L., and Lee, B.J. (2016). Hypothalamic TLR2 triggers sickness behavior via a microglia-neuronal axis. Sci. Rep. *6*, 29424.

Kaelberer, M.M., Buchanan, K.L., Klein, M.E., Barth, B.B., Montoya, M.M., Shen, X., and Bohórquez, D.V. (2018). A gut-brain neural circuit for nutrient sensory transduction. Science *361*, eaat5236.

Kenneth, N.S., Younger, J.M., Hughes, E.D., Marcotte, D., Barker, P.A., Saunders, T.L., and Duckett, C.S. (2012). An inactivating caspase 11 passenger mutation originating from the 129 murine strain in mice targeted for c-IAP1. Biochem. J. *443*, 355–359.

Khoury-Hanold, W., Yordy, B., Kong, P., Kong, Y., Ge, W., Szigeti-Buck, K., Ralevski, A., Horvath, T.L., and Iwasaki, A. (2016). Viral Spread to Enteric Neurons Links Genital HSV-1 Infection to Toxic Megacolon and Lethality. Cell Host Microbe *19*, 788–799.

Kigerl, K.A., Gensel, J.C., Ankeny, D.P., Alexander, J.K., Donnelly, D.J., and Popovich, P.G. (2009). Identification of two distinct macrophage subsets with divergent effects causing either neurotoxicity or regeneration in the injured mouse spinal cord. J. Neurosci. *29*, 13435–13444.

Koomoa, D.L., Geerts, D., Lange, I., Koster, J., Pegg, A.E., Feith, D.J., and Bachmann, A.S. (2013). DFMO/eflornithine inhibits migration and invasion downstream of MYCN and involves p27Kip1 activity in neuroblastoma. Int. J. Oncol. *42*, 1219–1228.

Kulkarni, S., Micci, M.A., Leser, J., Shin, C., Tang, S.C., Fu, Y.Y., Liu, L., Li, Q., Saha, M., Li, C., et al. (2017). Adult enteric nervous system in health is maintained by a dynamic balance between neuronal apoptosis and neurogenesis. Proc. Natl. Acad. Sci. USA *114*, E3709–E3718.

Laranjeira, C., Sandgren, K., Kessaris, N., Richardson, W., Potocnik, A., Vanden Berghe, P., and Pachnis, V. (2011). Glial cells in the mouse enteric nervous system can undergo neurogenesis in response to injury. J. Clin. Invest. *121*, 3412–3424.

Levy, M., Thaiss, C.A., Zeevi, D., Dohnalová, L., Zilberman-Schapira, G., Mahdi, J.A., David, E., Savidor, A., Korem, T., Herzig, Y., et al. (2015). Microbiota-Modulated Metabolites Shape the Intestinal Microenvironment by Regulating NLRP6 Inflammasome Signaling. Cell *163*, 1428–1443.

Mahar, M., and Cavalli, V. (2018). Intrinsic mechanisms of neuronal axon regeneration. Nat. Rev. Neurosci. *19*, 323–337.

Mawe, G.M. (2015). Colitis-induced neuroplasticity disrupts motility in the inflamed and post-inflamed colon. J. Clin. Invest. *125*, 949–955.

Mayo, L., Trauger, S.A., Blain, M., Nadeau, M., Patel, B., Alvarez, J.I., Mascanfroni, I.D., Yeste, A., Kivisäkk, P., Kallas, K., et al. (2014). Regulation of astrocyte activation by glycolipids drives chronic CNS inflammation. Nat. Med. *20*, 1147–1156.

Medzhitov, R., Schneider, D.S., and Soares, M.P. (2012). Disease tolerance as a defense strategy. Science *335*, 936–941.

Muller, P.A., Koscsó, B., Rajani, G.M., Stevanovic, K., Berres, M.L., Hashimoto, D., Mortha, A., Leboeuf, M., Li, X.M., Mucida, D., et al. (2014). Crosstalk between muscularis macrophages and enteric neurons regulates gastrointestinal motility. Cell *158*, 300–313.

Muller, P.A., Schneeberger, M., Kerner, Z., Wang, P., Ilanges, A., Matheis, F., del Mamol, J., Castro, T.B.R., Perkins, M., Han, W., et al. (2019). Microbes modulate sympathetic neurons via a gut-brain circuit. bioRxiv. https://doi.org/10.1101/545806.

Obata, Y., and Pachnis, V. (2016). The Effect of Microbiota and the Immune System on the Development and Organization of the Enteric Nervous System. Gastroenterology *151*, 836–844.

Ohman, L., and Simrén, M. (2010). Pathogenesis of IBS: role of inflammation, immunity and neuroimmune interactions. Nat. Rev. Gastroenterol. Hepatol. *7*, 163–173.

Parkhurst, C.N., Yang, G., Ninan, I., Savas, J.N., Yates, J.R., 3rd, Lafaille, J.J., Hempstead, B.L., Littman, D.R., and Gan, W.B. (2013). Microglia promote learning-dependent synapse formation through brain-derived neurotrophic factor. Cell *155*, 1596–1609.

Pavlov, V.A., Chavan, S.S., and Tracey, K.J. (2018). Molecular and Functional Neuroscience in Immunity. Annu. Rev. Immunol. *36*, 783–812.

Prüss, H., Tedeschi, A., Thiriot, A., Lynch, L., Loughhead, S.M., Stutte, S., Mazo, I.B., Kopp, M.A., Brommer, B., Blex, C., et al. (2017). Spinal cord injury-induced immunodeficiency is mediated by a sympathetic-neuroendocrine adrenal reflex. Nat. Neurosci. *20*, 1549–1559.

Rao, M., Rastelli, D., Dong, L., Chiu, S., Setlik, W., Gershon, M.D., and Corfas, G. (2017). Enteric Glia Regulate Gastrointestinal Motility but Are Not Required for Maintenance of the Epithelium in Mice. Gastroenterology *153*, 1068–1081.e7.

Salgo, B., Schmitz, A., Henze, G., Stutz, K., Dullenkopf, A., Neff, S., Gerber, A.C., and Weiss, M. (2006). Evaluation of a new recommendation for improved cuffed tracheal tube size selection in infants and small children. Acta Anaesthesiol. Scand. *50*, 557–561.

Salter, M.W., and Stevens, B. (2017). Microglia emerge as central players in brain disease. Nat. Med. *23*, 1018–1027.

Sanz, E., Yang, L., Su, T., Morris, D.R., McKnight, G.S., and Amieux, P.S. (2009). Cell-type-specific isolation of ribosome-associated mRNA from complex tissues. Proc. Natl. Acad. Sci. USA *106*, 13939–13944.

Shaw, T.N., Houston, S.A., Wemyss, K., Bridgeman, H.M., Barbera, T.A., Zangerle-Murray, T., Strangward, P., Ridley, A.J.L., Wang, P., Tamoutounour, S.,

et al. (2018). Tissue-resident macrophages in the intestine are long lived and defined by Tim-4 and CD4 expression. J. Exp. Med. *215*, 1507–1518.

Shechter, R., London, A., Varol, C., Raposo, C., Cusimano, M., Yovel, G., Rolls, A., Mack, M., Pluchino, S., Martino, G., et al. (2009). Infiltrating blood-derived macrophages are vital cells playing an anti-inflammatory role in recovery from spinal cord injury in mice. PLoS Med. *6*, e1000113.

Song, W.M., and Colonna, M. (2018). The identity and function of microglia in neurodegeneration. Nat. Immunol. *19*, 1048–1058.

Travagli, R.A., and Anselmi, L. (2016). Vagal neurocircuitry and its influence on gastric motility. Nat. Rev. Gastroenterol. Hepatol. *13*, 389–401.

Tsolis, R.M., Townsend, S.M., Miao, E.A., Miller, S.I., Ficht, T.A., Adams, L.G., and Bäumler, A.J. (1999). Identification of a putative Salmonella enterica serotype typhimurium host range factor with homology to IpaH and YopM by signature-tagged mutagenesis. Infect. Immun. *67*, 6385–6393.

Vanden Berghe, T., Hulpiau, P., Martens, L., Vandenbroucke, R.E., Van Wonterghem, E., Perry, S.W., Bruggeman, I., Divert, T., Choi, S.M., Vuylsteke, M., et al. (2015). Passenger Mutations Confound Interpretation of All Genetically Modified Congenic Mice. Immunity *43*, 200–209.

Veiga-Fernandes, H., and Mucida, D. (2016). Neuro-Immune Interactions at Barrier Surfaces. Cell *165*, 801–811.

Wang, Y., Cella, M., Mallinson, K., Ulrich, J.D., Young, K.L., Robinette, M.L., Gilfillan, S., Krishnan, G.M., Sudhakar, S., Zinselmeyer, B.H., et al. (2015). TREM2 lipid sensing sustains the microglial response in an Alzheimer's disease model. Cell *160*, 1061–1071.

White, J.P., Xiong, S., Malvin, N.P., Khoury-Hanold, W., Heuckeroth, R.O., Stappenbeck, T.S., and Diamond, M.S. (2018). Intestinal Dysmotility Syndromes following Systemic Infection by Flaviviruses. Cell *175*, 1198–1212.e12.

Xue, J., Sharma, V., Hsieh, M.H., Chawla, A., Murali, R., Pandol, S.J., and Habtezion, A. (2015). Alternatively activated macrophages promote pancreatic fibrosis in chronic pancreatitis. Nat. Commun. *6*, 7158.

Zeisel, A., Hochgerner, H., Lonnerberg, P., Johnsson, A., Memic, F., van der Zwan, J., Haring, M., Braun, E., Borm, L.E., La Manno, G., et al. (2018). Molecular Architecture of the Mouse Nervous System. Cell *174*, 999–1014.e22.

STAR★METHODS

KEY RESOURCES TABLE

REAGENT or RESOURCE	SOURCE	IDENTIFIER
Antibodies		
Human polyclonal anti-Hu (ANNA-1)	Gift of V. Lennon	N/A
Rat monoclonal anti-MHC class II	Millipore Sigma	Cat#: MABF33; RRID: AB_10807702
Rat monoclonal anti-Somatostatin	Merck	Cat#: MAB354; RRID: AB_2255365
Rabbit monoclonal anti-nNOS	Abcam	Cat#: ab76067, RRID: AB_2152469
Rabbit polycolonal anti-ASC	Adipogen	Cat#: AG-25B-0006; RRID: AB_2490440
Rabbit monoclonal anti-HA	Cell Signaling Technology	Cat#: 3724; RRID: AB_1549585
Rabbit monoclonal S100 beta		Cat#: ab52642; RRID: AB_882426
Rat monoclonal anti-CSF1R (AFS98)	Gift of M. Merad (MSSM)	AFS98; RRID: CVCL_KA99
Anti-CD45.2	BD-PharMingen	Cat#: 560693; RRID: AB_1727491
Anti-CD45R	BD-PharMingen	Cat#: 553088; RRID: AB_394618
Anti-CD103	eBioscience	Cat#: 11103185; RRID: AB_465177
Anti-CD11b	eBioscience	Cat#: 47011282; RRID: AB_1603193
Anti-CD11c	Affymetrix	Cat#: 48011482; RRID: AB_1548654
Anti-F4/80	Affymetrix	Cat#: 12480180; RRID: AB_465923
Anti-Siglec F	BD-PharMingen	Cat#: 562680; RRID: AB_2687570
Anti-CD3e	Thermo Fisher Scientific	Cat#: 45003180
Anti-Ly6G	BD-PharMingen	Cat#: 560601; RRID: AB_1727562
Anti-CD64	Biolegend	Cat#: 139309; RRID: AB_2562694
Anti-MHC II	Thermo Fisher Scientific	Cat#: 17532380
Aqua fixable dead cell stain	Invitrogen	Cat#: L34966
Bacterial and Protozoan Strains		
S. enterica serovar Typhimurium (SL1344)	UC Davis, Andreas Bäumler	Strain# SL1344; NCBI Taxonomy ID: 216597
S. enterica serovar Typhimurium (SL1344) *ΔspiB*	UC Davis, Andreas Bäumler	N/A
Yersinia pseudotuberculosis	NIH, Yasmine Belkaid	N/A
Toxoplasma gondii (me49)	UMass, Ricardo Gazzinelli	me49
Trypanosoma cruzi (Y strain)	UMass, Ricardo Gazzinelli	N/A
Strongyloides venezuelensis	Stanford, S. Galli	N/A
Chemicals, Peptides, and Recombinant Proteins		
Compound 21	Hello Bio	Cat#: HB6124
Tamoxifen	Sigma	Cat#: T5648
Ampicillin sodium salt	Sigma	Cat#: A0166
Neomycin trisulfate salt hydrate	Sigma	Cat#: N6386
Vancomycin hydrochloride	Sigma	Cat#: V2002
Metronidazole	Sigma	Cat#: M3761
Salbutamol sulfate	Selleck Chemicals	Cat#: S2507
Methylcellulose	Sigma-Aldrich	Cat#: 274429
Carmine Red	Sigma-Aldrich	Cat#: C1002
Spermine	Sigma-Aldrich	Cat#:85590
DFMO	Gift of P. Woster	N/A
zVAD-FMK	Selleck Chemicals	Cat#: S7023
TRIzol Reagent	Thermo Fisher Scientific	*Cat#: 15596026*
Streptomycin sulfate	Sigma-Aldrich	Cat#: S9137

(*Continued on next page*)

Continued

REAGENT or RESOURCE	SOURCE	IDENTIFIER
HBSS, calcium, magnesium	GIBCO	Cat# 24020117
HBSS, no calcium, no magnesium	GIBCO	Cat# 14170112
Dulbecco's Phosphate Buffered Saline	Corning	Cat# 21040CV
EDTA (0.5 M), pH 8.0	Ambion	Cat# AM9260G
RPMI 1640 Medium	GIBCO	Cat# 11875119
Collagenase VIII	Sigma-Aldrich	Cat# C2139
DNase I	Roche	Cat# 04536282001
Isoflurane (IsoThesia)	Henry Schein	Cat# 029405
DL-Dithiothreitol (DTT)	Sigma-Aldrich	Cat# D0632
Triton X-100	Alfa Aesar	Cat# A16046
Dimethyl sulfoxide (DMSO)	Sigma-Aldrich	Cat# D8418
Tween 20	Promega	Cat# H5151
Heparin	Sigma-Aldrich	Cat# H3149
Cuprolinic Blue	Polysciences	Cat#: 17052-100
DNA extraction buffer	Lucigen	Cat#: QE09050
RNAscope probe *Nlrp6*	ACDbio	Cat#: 404561
RNAscope probe *Elavl4*	ACDBio	Cat#: 479581-C2
PFHM-II	Thermo Fisher Scientific	Cat#: 12040077
Dialysis Tubing	Spectrum Labs	Cat#: 132676
Penicillin/streptomycin 100x	GIBCO	Cat#: 15140-122
Bioreactor Flask	Wheation	Cat#: WCL-1000-3
1M Tris-HCL pH 8	Invitrogen	Cat#: 15568-025
IgG Binding Buffer	Thermo Fisher Scientific	Cat#: 21011
IgG Elution Buffer	Thermo Fisher Scientific	Cat#: 21004
Protein G Sepharose	GE Healthcare	Cat#: 45-000-116
Gravity Column	Bio-Rad	Cat#: 7371512
30K - Centrifugal Filters	Amicon	Cat#: UFC903024
IgG from Rat Serum	Sigma-Aldrich	Cat#: I4131
Critical Commercial Assays		
Mouse Lipocalin-2/NGAL DuoSet ELISA	R&D Systems	Cat#: DY1857
PicoPure RNA Isolation Kit	Thermo Fisher Scientific	Cat#: KIT0204
RNAscope Kit	ACDBio	Cat#: 320850
Deposited Data		
Data generated by RNA sequencing are deposited in the NCBI Gene Expression Omnibus (GEO) database.	NCBI	GSE140309
Experimental Models: Organisms/Strains		
Mouse: C57BL6/J	Jackson Laboratory	#000664
Mouse: *Lyz2*^{Cre}	Jackson Laboratory	#004781
Mouse: *Rosa26*^{tdTomato}	Jackson Laboratory	#007914
Mouse: VGLUT2^{Cre}	Jackson Laboratory	#016963
Mouse: 129S1/SvImJ	Jackson Laboratory	#002448
Mouse: *Ccr2*$^{-/-}$	Jackson Laboratory	#004999
Mouse: *Casp1*$^{-/-}$ *Casp11*$^{-/-}$	Jackson Laboratory	#016621
Mouse: CBA/J	Jackson Laboratory	#000656
Mouse: *Rpl22*^{HA}	Jackson Laboratory	#011029
Mouse: *Snap25*^{Cre}	Jackson Laboratory	#023525
Mouse: *Adrb2*^{flox}	G. Karsenty	N/A
Mouse: *Arg1*^{flox}	Jackson Laboratory	#008817

(*Continued on next page*)

Continued

REAGENT or RESOURCE	SOURCE	IDENTIFIER
Mouse: *Cx3cr1*^{GFP}		N/A
Mouse: *Nestin*^{GFP}	P. Frenette, G. Enikolopov	N/A
Mouse: *Casp11*$^{-/-}$	Jackson Laboratory	#024698
Mouse: R26-CAG-ASC-citrine	Jackson Laboratory	#030744
Mouse: NSG	Jackson Laboratory	#005557
Mouse: *Phox2b*^{cre}	Jackson Laboratory	# 016223
#Mouse: *Plp1*^{CreERT}	Jackson Laboratory	# 005975
Mouse: *Rosa26*^{DTA}	Jackson Laboratory	# 009669
Mouse: R26-hM4Di/mCitrine	Jackson Laboratory	# 026219
Mouse: *Sox10*^{CreERT2}	B. Gulbransen, V. Pachnis	N/A
Mouse: SNS^{cre}	R. Kuhner	N/A
Mouse: *Nlrp6*^{flox}	P. Rosenstiel	N/A
Mouse: *Casp11*^{flox}	KOMP	N/A
Oligonucleotides		
Casp11 forward 5′-AGGCATATCTATAATCCCTTCACTG-3′	IDT	N/A
Casp11 reverse 5′-GAATATATCAAAGAGATGACAAGAGC- 3′	IDT	N/A
Arg1 forward 5′-CTCCAAGCCAAAGTCCTTAGAG-3′	IDT	N/A
Arg1 reverse 5′-AGGAGCTGTCATTAGGGACATC-3′	IDT	N/A
Ym1 forward 5′-AGACTTGCGTGACTATGAAGCATT-3′	IDT	N/A
Ym1 reverse 5′-GCAGGTCCAAACTTCCATCCTC-3′	IDT	N/A
Rpl32 forward 5′-ACAATGTCAAGGAGCTGGAG-3′	IDT	N/A
Rpl32 reverse 5′-TTGGGATTGGTGACTCTGATG-3′	IDT	N/A
Nlrp6 E1 forward 5′-TTGACTGTCAGCAAGAGTCC-3′	IDT	N/A
Nlrp6 E1 reverse 5′-GGTGATCCTTTCTGGGCTAAA-3′	IDT	N/A
Nlrp6 E4 forward 5′-CAGACGCTGTGGACCTTGT-3′	IDT	N/A
Nlrp6 E4 reverse 5′- ACGTGCTCGCGGTACTTCTT-3′	IDT	N/A
Elavl4 forward 5′-GATCAGGGATGCTAACCTGTATG-3′	IDT	N/A
Elavl4 reverse 5′- GGTGATGATGCGACCGTATT −3′	IDT	N/A
Recombinant DNA		
AAV9-hSyn-eGFP-WPRE-bGH	Addgene	#105539-AAV9
AAV9-hSyn-HI-eGFP-Cre-WPRE-SV40	Addgene	#105540-AAV9
Software and Algorithms		
GraphPad Prism version 8 for MacOS	Graphpad Software	https://www.graphpad.com
RStudio	RStudio	https://www.rstudio.com/
DEseq2	Bioconstructor	https://bioconductor.org/packages/release/bioc/html/DESeq2.html
Imaris (v. 8.4)	Bitplane	N/A
Fiji	ImageJ	https://imagej.net/Welcome
Microsoft Excel for MacOS	Microsoft	https://products.office.com/en-us/excel
Other		
Salmonella Shigella Agar (SS Agar)	BD	Cat# 211597
Luria's Broth base (LB)	Thermo-Fisher Scientific	Cat# 12795027
O.C.T. Compound (Tissue-Plus)	Fisher Healthcare	Cat# 23-730-571

LEAD CONTACT AND MATERIALS AVAILABILITY

Further information and requests for resources and reagents should be directed to and will be fulfilled by the Lead Contact, Daniel Mucida (mucida@rockefeller.edu). Mouse lines generated in this study are available with a completed Material Transfer Agreement.

EXPERIMENTAL MODEL AND SUBJECT DETAILS

Mice

C57BL/6J (000664), *Casp1*$^{-/-}$ *Casp11*$^{-/-}$(B6N.129S2-Casp1tm1Flv/J, 016621), CCR2$^{-/-}$ (B6.129S4-*Ccr2*^{tm1Ifc}/J, 004999), LysM^{Cre} (B6.129P2-*Lyz2*$^{tm1(cre)Ifo}$/J), *Arg1*$^{flox/flox}$ (C57BL/6-*Arg1*^{tm1Pmu}/J), Rosa26^{tdTomato} (B6.Cg-Gt(ROSA)26Sor$^{tm14(CAG-tdTomato)Hze}$/J), VGLUT2^{Cre} (*Slc17a6*$^{tm2(cre)Lowl}$/J), *Rpl22*^{HA} (B6N.129-Rpl22$^{tm1.1Psam}$/J), 129S1(129S1/SvImJ), CBA/J, *Cx3cr1*^{GFP}(*Cx3cr1*$^{tm1Litt/LittJ}$), *Phox2b*^{cre} (B6(Cg)-Tg(Phox2b-cre)3Jke/J), *Snap25*^{Cre}(*Snap25*$^{tm2.1(cre)Hze}$), NSG (NOD.Cg-*Prkdc*^{scid}*Il2rgtm1*^{Wjl}/SzJ), *Casp11*$^{-/-}$ (Casp4tm1Yuan/J), and R26-CAG-ASC-citrine (B6.Cg-Gt(ROSA)26Sortm1.1(CAG-Pycard/mCitrine*,-CD2*)Dtg/J), *Plp1*^{creERT} (B6.Cg-Tg(Plp1-cre/ERT)3Pop/J), *Rosa26*$^{lsl\text{-}hM4Di}$ (B6N.129-*Gt(ROSA)26Sor*$^{tm1(CAG-CHRM4*,-mCitrine)Ute}$), and ROSA-DTA (B6.129P2-*Gt(ROSA)26Sortm1(DTA)*Lky/J) were purchased from The Jackson Laboratories and maintained in our facilities. SNS^{cre} (Tg(*Scn10a*^{cre})1Rkun were a gift of R. Kuhner, *Nestin*^{GFP} (Tg(Nes-EGFP)33Enik were generously provided by P. Frenette and G. Enikolopov, *Adrb2*$^{flox/flox}$ (Adrb2^{tm1Kry}) by G. Karsenty, Sox10^{CreERT2} (Tg(Sox10-icre/ERT2)26Vpa) were generously provided by B. Gulbransen and V. Pachnis, *Nlrp6*$^{flox/flox}$ by P. Rosenstiel (targeting of Exon 1 of *Nlrp6*, frozen sperm generously provided by T. Kanneganti), and *Casp11*$^{flox/flox}$ by KOMP and A. Wullaert. Mouse lines were interbred in our facilities to obtain the final strains described in the text. Genotyping was performed according to the protocols established for the respective strains by The Jackson Laboratories or personal communication with the donating investigators. Mice were maintained at the Rockefeller University animal facilities under specific pathogen-free conditions. Mice were fed a standard chow diet and used at 7–12 weeks of age for most experiments. Animal care and experimentation were consistent with NIH guidelines and were approved by the Institutional Animal Care and Use Committee at the Rockefeller University.

Microorganisms

Salmonella enterica serovar Typhimurium (SL1344) and its mutant *spiB* were used for infection experiments and cultured prior to infection as described below. *Yersinia pseudotuberculosis* (IP32777) was cultured prior to infection as described below. *S. venezuelensis* was maintained in our facility by periodically infecting NSG mice and culturing larvae as described below. *Toxoplasma gondii* was maintained in our lab by periodically infecting C57BL/6 mice with 5 cysts administrated intraperitoneally (i.p.). Cysts were isolated from brain tissue 30 days after infection. *Trypanosoma cruzi*. The *T. cruzi* Y strain was maintained by serial passage from mouse to mouse.

METHOD DETAILS

Infections

Salmonella enterica *Typhimurium*

For infections with *Salmonella spiB*, mice were pre-treated with a single dose of Streptomycin (20 mg/mouse dissolved in 100 μl of DPBS) administered by oral gavage 18-24 h prior to infection Mice were then orally inoculated with 10^9 CFU of *spiB*. For *Salmonella* re-infection experiments, mice were subjected to *spiB* infection as described above. 1 week post-clearance of *spiB* from the feces, mice were fasted for 4 h and infected with 10^6 CFU of wild-type *Salmonella enterica* Typhimurium (SL1344). For all *Salmonella* infections, a single aliquot of either strain of *Salmonella* was grown in 3 mL of LB overnight at 37°C with agitation. Bacteria were then sub-cultured (1:300) into 3 mL of LB for 3.5 h at 37°C with agitation, and diluted to final concentration in 1 mL of DPBS. Bacteria were inoculated by gavage into recipient mice in a total volume of 100 μl. For experiments using heat-killed *spiB*, samples subjected to heat treatment (95°C for 10 min in water bath), prior to gavage and successful inactivation was confirmed by plating a serial dilution made from the suspension and then 5 μL onto Salmonella-Shigella plates.

Yersinia pseudotuberculosis

Y. pseudotuberculosis (strain IP32777) was grown as previously described with some adjustments (Fonseca et al., 2015). Briefly a single aliquot of the strain was grown in 3 mL of 2xYT media overnight at 28°C with vigorous agitation. Mice were fasted for 12 h prior to infection with 10^8 CFU by oral gavage.

For heterologous re-infection experiments, mice infected with *spiB* or *Y. pseudotuberculosis* as described above were subjected to either 10^8 of *Y. pseudotuberculosis* or 10^9 CFU of *Salmonella spiB* on day 21 days post-infection with *spiB* or *Y. pseudotuberculosis* infection, and sacrificed 10 days post-secondary infection.

Strongyloides venezuelensis

S. venezuelensis was maintained in our facility in NSG mice by subcutaneous infection with 700 larvae, resulting in chronic infection of this strain. For each experiment, feces of infected NSG mice were collected and spread on Whatman paper, which was placed into a beaker with water and incubated at 28°C. The hatching larvae were collected over 2-3 days. Mice were infected subcutaneously with 700 larvae/100 μl water per mouse. *S. venezuelensis* was passaged by periodically infecting naive adult NSG mice.

Toxoplasma gondii

T. gondii was maintained in the lab by periodically infecting mice administered by intraperitoneal injection of 5 cysts/mouse in a total volume of 100 μl of DPBS.

Trypanosoma cruzi (T. cruzi, Y strain)

For each experiment, blood from an infected mouse was collected, parasites were quantified and naive recipient mice infected by intraperitoneal injection of 10^4 parasites. Infected mice were sacrificed for tissue analysis at day 22 post-infection, when the parasite load reaches a plateau (Arantes et al., 2004).

Antibodies and flow cytometry

Antibodies used for whole-mount immunofluorescence imaging

The following primary antibodies were used, and unless otherwise indicated concentrations apply to all staining techniques: Somatostatin (1:200, Millipore Sigma, MAB354), ANNA-1 (1:200,000, Gift of Dr. Vanda A. Lennon), HA (1:400, Cell Signaling Technologies, 3724S), nNOS (1:200, ABCAM, ab76067), MHC II (1:400, Millipore Sigma, MABF33), S100 beta (1:200, Abcam, ab52642), ASC (1:200, Adipogen, AL177), GFP (1:400, Nacalai, GF090R). Fluorophore-conjugated secondary antibodies were either H&L or Fab (Thermo Fisher Scientific) at a consistent concentration of 1:400 in the following species and colors: Goat anti-rabbit (AF488/568/647), goat anti-rat (AF488/647), goat anti-chicken (AF488/568/647), goat anti-human (AF568/647),

Antibodies used for cell sorting of intestinal macrophages

Fluorescent-dye-conjugated antibodies were purchased from BD-PharMingen (USA) (anti-CD45.2, 104; anti-CD45R, RA3-6B2); eBioscience (USA) (anti-CD103, 2E7; anti-MHC II, M5; anti-F4/80, BM8; anti-CD11b, M1/70; anti-CD11c, N418; anti-Siglec F, E50-2440; anti-CD3e,145-2C11; anti-Ly6G, RB6-8C5) or BioLegend (USA) (anti-CD64 X54-5/7.1). Live/Dead staining was performed using Aqua fixable dead cell stain (Invitrogen). Macrophages were sorted as Aqua–CD45+Lin–(CD3–B220–Siglec F–LY6G–) MHCII+F4/80+CD11B+CD11C+CD103–) using a FACS Aria cell sorter flow cytometer (Becton Dickinson).

Intestine dissection

Mice were sacrificed and duodenum (1 cm moving distal from the gastroduodenal junction), ileum (1 cm moving proximal from the ileocecal junction), or colon (4 cm moving proximal from the rectum) was removed. For dissection of the *muscularis*, following the above procedures, the intestinal tissue was placed on a chilled aluminum block with the serosa facing up (Gabanyi et al., 2016). Curved forceps were then used to carefully remove the *muscularis*.

Nodose ganglion dissection

Mice were sacrificed and the ventral neck surface was cut open. Associated muscle was removed by blunt dissection to expose the trachea and the nodose ganglion was then located by following the vagus nerve along the carotid artery to the base of the skull. Fine scissors were used to cut the vagus nerve below the nodose ganglion and superior to the jugular ganglion.

Intestine motility measurements

For measurement of total intestinal transit time, mice were given an oral gavage of 6% carmine red (Sigma-Aldrich) dissolved in 0.5% methylcellulose (prepared in with sterile 0.9% NaCl). Total intestinal transit time was measured as the time from oral gavage it took for mice to pass a fecal pellet that contained carmine. Experiments were ended after 450 min.

Ileal smooth muscle contractility

Ileal ring tension was assessed by organ bath (Radnoti) myography as previously described (Muller et al., 2014). Briefly, distal ileal rings were mounted and equilibrated for one h and were distended to 0.5 g followed by 10 min of relaxation. The data was acquired using the PowerLab acquisition system and analyzed using LabChart Software (AD Instruments).

Lipocalin-2 ELISA

Lipocalin-2 levels in fecal samples were quantified using a Mouse Lipocalin-2 ELISA kit (R&D Systems) according to manufacturer's instructions.

Drug Administration

Salbutamol

Salbutamol sulfate (Selleck Chemicals) was dissolved in sterile NaCl to a concentration of 56 mg/mL, loaded into osmotic pumps and administered by subcutaneous osmotic pumps implanted as described below at a final dose of 400 μg/day for 14 days.

Pan caspase inhibition

zVAD-FMK (Selleck Chemicals) was dissolved in DMSO and administered at a dose of 50 μg/mouse by daily intraperitoneal injections over the course of a 7-day infection starting 1 day prior to infection.

Polyamine administration

Spermine (Sigma-Aldrich) was administered at a concentration of 2% in drinking water. Spermine-substituted drinking water was changed daily and fluid intake was monitored. Treatment was started 3 days prior to infection with *Salmonella spiB* and continued over the course of experiments.

ODC1 inhibition

Difluoromethylornithine (DFMO, gift from P. Woster, MSSM) was dissolved in tap water, filter-sterilized, and administered at a concentration of 4% in drinking water. DFMO-substituted water was changed daily, and fluid intake was monitored. Treatment was started 4 days prior to infection with *Salmonella spiB* and continued over the course of experiments.

Isoflurane induction

A plexiglass induction chamber was placed on a heating pad set to 37°C. Isoflurane was set at 1% with an oxygen flow of 1 L/minute. Mice were placed in the induction chamber and monitored for loss of movement, after which a period of 15 min was elapsed. Respiration was monitored continuously during this period. Following isoflurane treatment, mice were returned to their home cage for a period of 1 h prior to receiving Streptomycin pre-treatment, followed by *spiB* infection as described above.

Sham intraperitoneal injections

Sham intraperitoneal injections of DPBS or IgG (isotype control from MM depletion experiments, see below) were performed by mimicking the anti-CSF1R MM depletion protocol, by intraperitoneal injection of 200 μl of DPBS or IgG/ mouse (100 μl/flank). Injections were performed 12 h prior to *spiB* infection, and an additional injection was performed at day 3.5 post-infection. Mice were sacrificed and tissue was analyzed at 7 days post-infection.

Subcutaneous pump implantation

Mice were anesthetized using isoflurane and, under sterile conditions, a small incision was made on the dorsal side of the neck. An Alzet pump (Model 1002) filled with Salbutamol sulfate prepared as described above was placed under the skin and moved back toward the right flank. The incision was then closed with surgical wound clips (Kent Scientific). Mice were then left to rest for 7 days before infection with *spiB*.

Adrenalectomy

Mice were anesthetized using isoflurane and, under sterile conditions, bilateral incisions were made dorsally just below the rib cage. The adrenal glands were then grasped by forceps from the suprarenal blood vessels and extracted from the surrounding tissue. Care was taken to minimize any bleeding before the muscle incision was closed with absorbable sutures. Surgical wound clips were then used to close the skin. Mice were then kept on 0.9% saline drinking water for 9 days prior to infection with *spiB*.

Generation of *Nlrp6*$^{flox/flox}$ mice

The *Nlrp6*$^{flox/flox}$ strain was generated by Flp-Neo-mediated insertion of loxP sites flanking exon 1 of the *Nlrp6* locus. ES cells were used to generate the conditional knockout allele. The strain was generated in collaboration with genoWay (Lyon, France).

16S sample processing

16S samples were processed utilizing a Promega Maxwell® RSC 48 Instrument. Following RNA extraction from all samples, samples were quantified using a ThermoFisher Quant-It dsDNA High-Sensitivity Kit on a microplate reader.

16S sequencing

16S sequencing was performed on either the Illumina HiSeq 2500 or the Illumina MiSeq depending on project-specific needs. Raw paired-end fastq files containing sequence reads were merged at the overlapping region to produce a single 16S contig. All merged sequences having more than 1 expected error per read were filtered. Operational taxonomic units (OTU) were generated by clustering sequences with a 99% correspondence and chimera sequences were removed using usearch (Edgar, 2010) (v11).

Chemogenetics

Mice expressing hM4Di in relevant neuronal populations were injected with 10mg/kg Compound 21 (HelloBio) 24 h prior to oral gavage with *spiB*.

Antibiotic-mediated microbiota depletion and re-colonization

7 days post-oral gavage with *spiB* mice were given drinking water supplemented with 10 g/L Splenda (artificial sweetener, control), or broad-spectrum antibiotics (1g/L ampicillin, 0.5g/L vancomycin, 1g/L neomycin, 0.5g/L metronidazole) in the drinking water supplemented with 10 g/L Splenda for 2 weeks. Mice on antibiotics were then put onto Splenda-containing water and all mice were given feces from an uninfected cage of age-matched C57BL/6J mice. All tissues were then harvested 2 weeks after recolonization.

Anti-CSF1R (ASF98) antibody production

Anti-CSF1R was produced by suspension culture of the ASF98 hybridoma cell line (gift from Miriam Merad). Cells were thawed and passaged twice (1:10) in PFHM-II (Thermo Fisher) media supplemented with P/S (Thermo Fisher). Cells were then seeded at $5x10^6$ in 15 mL of PFHM-II in the cellular compartment of a 1000 mL bioreactor (Wheaton) and allowed to grow for 7-10 days. The cell

compartment was then harvested, spun down and the supernatant collected. Supernatant was filtered and antibody was purified from the supernatant by affinity purification using protein G Sepharose (GE Healthcare) in a gravity column (Bio-Rad). Briefly, the protein G was equilibrated with 100 mL binding buffer (Thermo Fisher Scientific) and supernatant was loaded onto and run through the column. The column was then washed with 200 mL of binding buffer and eluted with 10 mL elution buffer (Thermo Fisher Scientific). Antibody was eluted in fractions directly into 100 μl 1 M Tris-HCL pH 8 (Invitrogen) and the concentrations were measured on a Nanodrop 2000 spectrophotometer (Thermo Fisher Scientific). Fractions were combined and dialyzed in 2 L DPBS for 2 days at 4°C using 14,000 MWCO dialysis tubing (Spectrum Labs) changing once. The antibody was then concentrated using centrifugal filters (30,000 MW, Amicon) and stored at 4°C until use.

MM depletion using anti-CSF1R

Anti-CSF1R was diluted in sterile DPBS to a final concentration of 6.25 mg/mL and 50 mg/kg of anti-CSF1R or isotype control (IgG from rat serum, Sigma-Aldrich) were administered by i.p. injections. Mice were previously habituated to i.p. injections for at least 5 days prior to the start of depletion and *spiB* infection. For all experiments, depletion was performed twice over the course of 7 days (day 0 and day 3.5). For infection experiments, depletion was performed 12 h prior to infection. Animals were then subjected to the *Salmonella spiB* infection protocol as described above, and received and additional dose of either anti-CSF1R or isotype control 3.5 days after the initial dose. Animals were sacrificed at 7 dpi and intestinal tissue dissected for analysis.

Immunocytochemistry

Cuprolinic blue staining for visualization of enteric neurons was performed as previously described (Holst and Powley, 1995). The method was utilized for quantification of enteric neurons in *T. gondii* and *T. cruzi* infection experiments (Figure S1).

Whole-mount intestine immunofluorescence

Briefly, mice were sacrificed by cervical dislocation and the small intestine was removed and placed in HBSS $Mg^{2+}Ca^{2+}$(GIBCO) + 5% FCS. The intestine was cut open longitudinally and the luminal contents washed away in DPBS. The *muscularis* was then carefully dissected away from the underlying mucosa in one intact sheet. The tissue was pinned down in a plate coated with Sylgard and then fixed for O/N with 4% PFA with gentle agitation. After washing in DPBS whole mount samples were then permeabilized first in 0.5% Triton X-100/0.05% Tween-20/4 μg heparin (PTxwH) for 2 h at room temperature (RT) with gentle shaking. Samples were then blocked for 2 h in blocking buffer (PTxwH with 5% bovine serum albumin/5% donkey/goat serum) for 2 h at RT with gentle agitation. Antibodies were added to the blocking buffer at appropriate concentrations and incubated for 2 days at 4°C. After primary incubation the tissue was washed 4 times in PTxwH and then incubated in blocking buffer with secondary antibody at concentrations within the primary antibody range for 2 h at RT. Samples were again washed washed 4 times in PTxwH and then mounted with FluoroMount G on slides with 1 ½ coverslips. Slides were kept in the dark at 4°C until they were imaged.

Confocal imaging

Whole-mount intestine samples were imaged on an inverted LSM 880 NLO laser scanning confocal and multiphoton microscope (Zeiss) and on an inverted TCS SP8 laser scanning confocal microscope (Leica).

RiboTag

Heterozygous or homozygous $Snap25^{RiboTag}$ were used for TRAP-seq analysis as no differences were found between either genotype. For intestine immunoprecipitation (IP) mice were sacrificed and tissue remove and divided as above. Samples were washed of fecal contents in PBS with cycloheximide (0.2 mg/mL) (PBS/CHX). Mesenteric fat was removed and the *muscularis* was separated from the mucosa as described above and samples were washed 5 times in PBS/CHX. For nodose ganglion IP, tissues were isolated as described above. For $Snap25^{\Delta Nlrp6:RiboTag}$ animals, ileum *muscularis* was isolated as above and flash frozen in liquid nitrogen prior to immunoprecipitation. The RiboTag immunoprecipitation protocol (http://depts.washington.edu/mcklab/RiboTagIPprotocol2014.pdf) was then followed with the following modifications: All samples were homogenized by hand with a dounce homogenizer in 2.5 mL supplemented homogenization buffer (changes per 2.5 mL: 50 μl Protease Inhibitor, 75 μl heparin (100 mg/mL stock), 25 μl SUPERase In RNase Inhibitor). Samples were then centrifuged for 10 min at 10,000 G, after which 800 μl of supernatant was removed and 5 μL of anti-HA antibody (Abcam, ab9110) was added. For input samples, 40 μl of this supernatant was added to 60uL of PicoPure lysis buffer and stored at −80°C. Samples were kept rotating at 4°C with antibody for 1 h. 200 μl of Thermo Protein magnetic A/G beads were washed with homogenization buffer, added to the sample, and kept rotating for 30 min at 4°C. The beads were washed four times with high-salt buffer and samples were eluted with 100 μl of PicoPure lysis buffer. RNA was extracted using the Arcturus PicoPure RNA isolation kit (Applied Biosystems) according to the manufacturer's instructions.

RNA-sequencing

RNA libraries were prepared using SMARTer Ultra Low Input RNA (ClonTech Labs) and sequenced using 75 base-pair single end reads on a NextSeq 500 instrument (Illumina). Reads were aligned using Kallisto (Bray et al., 2016) to Mouse Ensembl v91. Transcript abundance files were then used in the DESeq2 R package, which was used for all downstream differential expression analysis and generation of volcano plots. Differentially expressed genes between samples were compared with a cutoff of $\log_2$ Fold Change > 1.

Mining of published iEAN scRNA-seq

The published single-cell analysis of the mouse nervous system at mousebrain.org/genesearch.html (PMID: 30096314) was searched for *Nrlp6* and filtered for clusters that express the gene at a trinarization score > = 0.95. Relative expression was then plotted as a heatmap in Prism 8. *Vglut2*+ subsets were defined based on the same single-cell analysis.

Cryosectioning of fresh-frozen tissue

Mice were given a lethal dose of isoflurane and then perfused with 30 mL ice cold DPBS. The ileum and colon were removed and flushed of luminal contents. The tissue was then transferred to OCT, positioned, flash frozen, moved to −20 for 2 h, and finally moved to −80 for long term storage. Prior to cryosectioning, OCT blocks were equilibrated in the cryostat for 20 min. Sections were cut at 15 μm, put onto SuperfrostPlus slides, and left to dry for 10-15 min. Slides were then transferred to dry ice and finally to −80°C before RNAscope® processing.

RNA fluorescence *in situ* hybridization (FISH) using RNAscope® technology

RNAscope® *in situ* hybridization was performed using probes against *Nlrp6* and *Elavl4* on 15 μm sections of fresh frozen ileum or colon tissue isolated from C57BL/6J mice according to the manufacturer's instruction with the following modification, tissue was pre-treated with Protease IV for 20 min at RT. Samples were then mounted in Fluoromount-G with DAPI and 1 ½ coverslips were applied.

Neuronal quantification

A minimum of 10 images were randomly acquired across a piece of whole-mount *muscularis*. These images were then opened in ImageJ, and the cell counter was used to count the number of ANNA-1+ cells in a given field. This number was then multiplied by a factor of 2.95 (20x objective) or 3.125 (25x objective), to calculate the number of counted neurons per square millimeter (mm^2). The average of 10 (or more) images was then calculated and plotted. Thus, every point on a given graph corresponds to a single animal. For determining iEAN subtype changes, the number of nNOS+, SST+, and tdTomato+ neurons were also counted. These numbers were then reported as both number per mm^2 and percent of ANNA-1+ neurons.

Macrophage intercalation calculation

Raw data as imported from the microscope was used for all cell identification and subsequent analyses. Some post –analysis pseudo-color adjustment was performed for individual images to account for differences in auto-fluorescence and labeling. *Imaris* (Bitplane AG) software was used for cell identification, using the "*Surfaces*" algorithm as described by the manufacturer. A surface was created based on anti-ANNA-1 (neuron) staining to define neuronal ganglia. A masked channel was then created to capture fluorescence in other channels within the neuronal ganglia volume. A second surface was created based on anti-MHCII (macrophage) staining only within the masked channel. Volume statistics on both neuron (total) and macrophage (neuronal ganglia masked) surfaces were then exported. Percent macrophage intercalation per image was calculated as:

$$\textit{Macrophage Intercalation} = \frac{(\sum(\textit{Macrophage surface volumes}) + \sum(\textit{Neuronal ganglia surface volumes})}{\sum(\textit{Neuronal ganglia surface volumes})} \times 100$$

The average of at least 10 random macrophage intercalation percentages was used to determine the percentage for each individual animal.

3D image reconstruction for MM ganglionic intercalation calculations

Images were adjusted post hoc using Imaris x64 software (version 9.1 Bitplane) and 3D reconstructions were recorded as mp4 video files. Optical slices were taken using the orthoslicer or oblique slicer tools.

Colony forming unit counting

Fecal pellets from *Salmonella spiB*-infected mice were weighed and then disrupted in 400 μL of DPBS. Serial dilutions were made from the original suspension and then 5 μL of each dilution was plated onto Salmonella-Shigella plates. The plates were then incubated overnight and the number of black colonies were counted for the serial dilution with the clearest delineation of single units. This number was then multiplied by the dilution factor and by 80 to give the number of colony forming units (CFU) in the original suspension. CFU numbers were then divided by the original fecal pellet weight to give the number of CFU per mg of feces.

Determination of caspase 11 mutation status by PCR and Sanger Sequencing

DNA was extracted from ear pieces of mice using QuickExtract DNA Extraction Solution (Lucigen). Target sequences were amplified using the following primers: Forward 5′-AGGCATATCTATAATCCCTTCACTG-3′; Reverse 5′-GAATATATCAAAGAGATGACAA GAGC- 3′. The following PCR conditions were used: 4 min 94°C, 1 min 94°C, 0.5 min 58°C, 1 min 72°C, 7 min 72°C, and end at 12°C. Samples were loaded on 3% agarose gels, and bands from all strains were compared to samples from C57BL/6J and 129S mice. The 5 bp deletion in *Casp11* described in the 129S1 strain fragment runs slightly higher than the wild-type fragment at a height of approximately 220 bp (Vanden Berghe et al., 2015). *Casp11* mutation status was further confirmed in C57BL/6J, CBA/J and 129S1 mice by Sanger sequencing of a gel-purified PCR product using primers 5′-CAGTATTATTATTGGTGATGCAAATG-3′

and 5′-GGAATATATCAAAGAGATGACAAGAGC-3′. *Casp11* mutation status was also confirmed in further relevant mouse strains utilized in this study.

Single Cell Suspension of Intestinal Macrophages

Mice were euthanized, and the small intestine was carefully removed, cleaned, cut open longitudinally and washed 2X in HBSS $Mg^{2+}Ca^{2}$GIBCO) and 1X in HBSS $Mg^{2+}Ca^{2}$ with 1 mM DTT (Sigma- Aldrich). The tissue was cut in two and the *muscularis* region was carefully dissected from the underlying mucosa. *Muscularis* tissue was then finely cut and digested in HBSS $Mg^{2+}Ca^{2+}$+ 5% FBS + 1x NaPyr + 25mM HEPES + 50 μg/mL DNase I (Roche) + 400 U/mL Collagenase D (Roche) + 2.5U/mL Dispase (Corning) at 37°C. The *muscularis* was digested for 40 min. The tissue was then homogenized with an 18-gauge needle, filtered through a 70 μm cell strainer and washed with HBSS $Mg^{2+}Ca^{2}$. Cells were incubated with Fc block and antibodies against the indicated cell surface markers in FACS buffer (PBS, 1% BSA, 10 mM EDTA, 0.02% NaN_3).

Quantitative PCR

Total RNA was isolated using TRIzol™ (Invitrogen), from which cDNA libraries were reverse transcribed using Superscript II (Invitrogen) and random primers following the instructions provided by the manufacturer. Quantitative PCR (qPCR) was performed using SYBR green (Bio-Rad Laboratories). Data were collected and analyzed on a QuantStudio 3 (Thermo Scientific). The *Rpl32* housekeeping gene was used to normalize samples. For TRAP-qPCR, RiboTag purified mRNA was reverse transcribed using iScript cDNA Synthesis Kit (BioRad) and qPCR was performed using SYBR green (Bio-Rad Laboratories). The following primers were used: *Rpl32* forward 5′-ACAATGTCAAGGAGCTGGAG-3′, *Rpl32* reverse 5′- TTGGGATTGGTGACTCTGATG-3′, *Arg1* forward 5′-CTCCAAGCCAAAGTCCTTAGAG- 3′, *Arg1* reverse 5′-AGGAGCTGTCATTAGGGACATC-3′, *Ym1* forward 5′-AGACTTGCGTGAC TATGAAGCATT-3′, *Ym1* reverse 5′-GCAGGTCCAAACTTCCATCCTC- 3′, *Nlrp6* exon 4 forward 5′-CAGACGCTGTGGACCTTGT-3′, *Nlrp6* exon 4 reverse 5′- ACGTGCTCGCGGTACTTCTT- 3′, *Nlrp6* exon 1 forward 5′-TTGACTGTCAGCAAGAGTCC-3′, *Nlrp6* exon 1 reverse 5′-GGTGATCCTTTCTGGGCTAAA-3′, *Elavl4* forward 5′-GATCAGGGATGCTAACCTGTATG-3′, *Elavl4* reverse 5′-GGTGATGATGCGACCGTATT-3′. To calculate a fold change, the final qPCR cycle of 45 was chosen in cases in which there was no amplification. This was comparable to water, which was used as a control and did not amplify.

AAV9 Transduction of iEAN

Casp11$^{flox/flox}$ mice were retro-orbitally injected with ~5 × 10^{11} GC of AAV9-hSyn-HI-eGFP-Cre-WPRE-SV40 (105540-AAV9) or AAV9-hSyn-eGFP-WPRE-bGH (Addgene #105539-AAV9) diluted in 100 μl of sterile DPBS. Mice were then infected at least 2 weeks post-viral injection.

Induction of glia depletion

Plp1^{CreERT};Rosa26^{DTA} (*Plp1*^{iDTA}, Cre+) and Rosa26^{DTA} mice (Cre-) received a single oral gavage of 8 mg tamoxifen (Sigma) solubilized in 250 μL sterile corn oil (Sigma) at 6-7 weeks of age. Mice were infected with Salmonella *spiB* 5 days post-tamoxifen administration and sacrificed at day 6 post-infection (day 11 post-tamoxifen).

QUANTIFICATION AND STATISTICAL ANALYSIS

Statistical analysis

Significance levels indicated are as follows: * $p < 0.05$, ** $p < 0.01$, *** $p < 0.001$, **** $p < 0.0001$. All data are presented as mean ± SD or mean ± SEM. At least two independent experiments were performed throughout in this study. All statistical tests used were two-tailed. The experiments were not randomized and no statistical methods were used to predetermine sample size. Multivariate data were analyzed by one-way ANOVA and Tukey's multiple comparisons post hoc test. Comparisons between two conditions were analyzed by unpaired Student's t test. GraphPad PRISM version 8.0 and R 3.4.3 were used for generation of graphs and statistics.

DATA AND CODE AVAILABILITY

Data resources

Data generated by RNA sequencing are deposited in the NCBI Gene Expression Omnibus (GEO) database and are accessible under GEO: GSE140309. All software used is available online, either freely or from a commercial supplier and is summarized in the Key Resources table. Algorithms described above are purely mathematical calculations and can be performed using any software.

Code resources

No new software was written for this project.

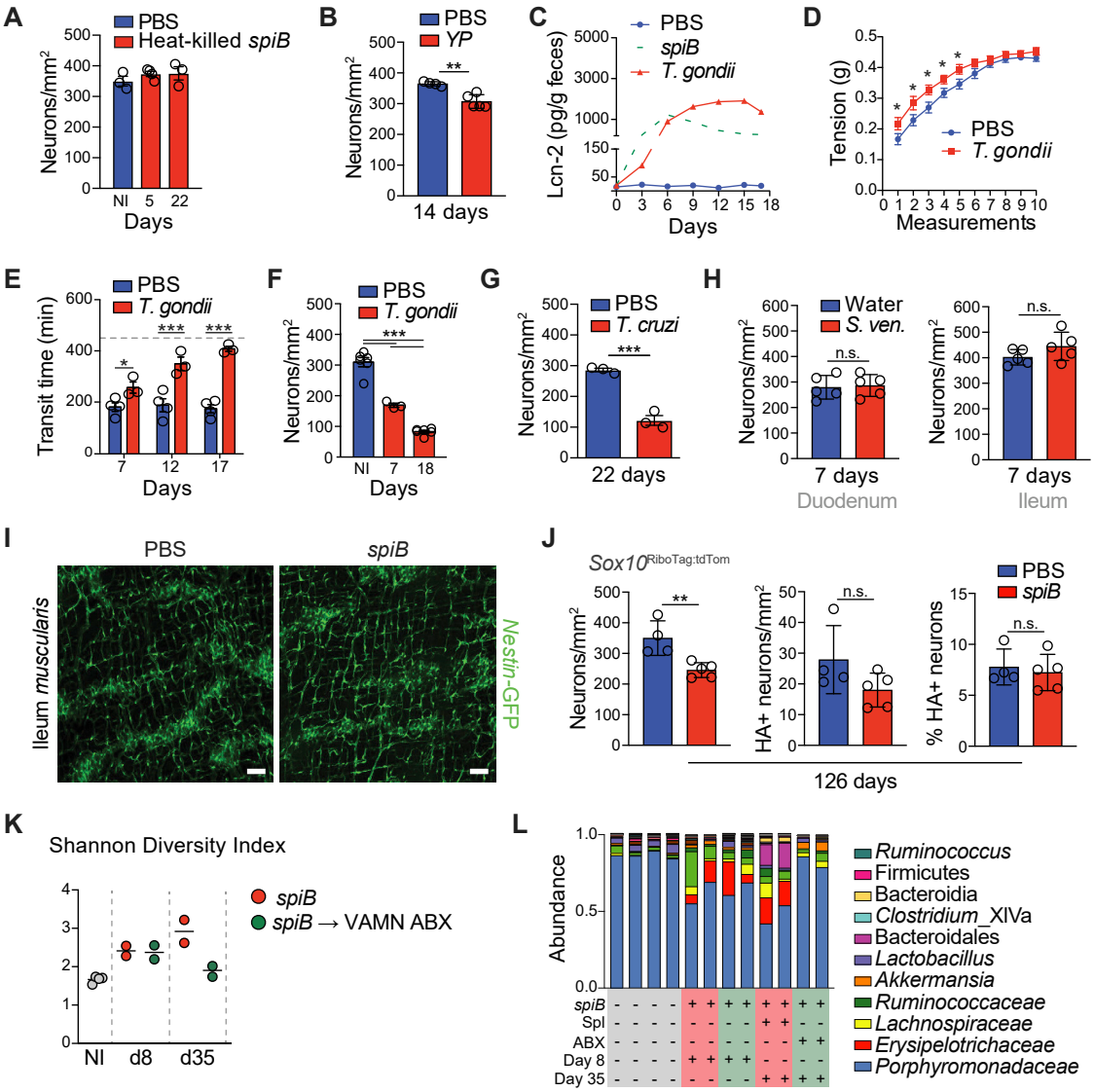

Figure S1. iEAN Loss is Pathogen Specific, Does Not Impact Potential Precursors, and Correlates with Dysbiosis, Related to Figure 1

(A) Neuronal quantification as assessed by immunofluorescence staining (ANNA-1) in the myenteric plexus of ileal segments from C57BL/6J mice on the indicated days post-exposure to 10^9 CFU of heat-killed *Salmonella spiB*. (B) Neuronal quantification (ANNA-1 staining) in the myenteric plexus of ileal segments from C57BL/6J mice orally infected with 10^8 CFU of *Y. pseudotuberculosis*. (C-F) C57BL/6J mice were orally infected with 5 cysts of *Toxoplasma gondii*. (C) Quantification of fecal Lcn-2 levels as assessed by ELISA on the depicted days; (D) Ileal ring myography assessed on day 18 post-infection; (E) Total gastrointestinal transit time as assessed on the indicated days post infection; experiments were ended at 450 min (dashed line); (F) Neuronal quantification as assessed by cuprolinic blue staining in the ileum myenteric plexus on the indicated days post infection. NI = non-infected. (G) Neuronal quantification as assessed by cuprolinic blue staining in the ileum myenteric plexus on the indicated days post-infection of C57BL/6J mice with 10^4 parasites of *T. cruzi*. (H) Neuronal quantification (ANNA-1 staining) in the myenteric plexus of (left panel) duodenal and (right panel) ileal segments C57BL/6J mice subcutaneously injected with 700 L3 larvae of *S. venezuelensis* (*S. ven.*), analyzed on day 8 post-infection. (I) Representative confocal immunofluorescence images of ileum muscularis from *Nestin*^{GFP} reporter mice 7 days post-oral exposure to PBS or *spiB*. Scale bars, 50 μm. Images representative of at least n = 5 animals per group. (J) Neuronal quantification and glial reporter overlap as assessed by immunofluorescence staining (ANNA-1, HA) in the ileal myenteric plexus from tamoxifen-treated *Sox10*^{RiboTag} reporter mice 126 days post oral-gavage with PBS or *spiB*. (K) Shannon diversity index of 16S sequencing from feces obtained from n = 2 mice in representative groups in Figure 1L. (L) Top 11 most abundant genera from 16S sequencing of feces obtained from mice in representative groups in Figure 1L. Unless otherwise indicated, data are representative of at least 3 mice per condition. At least 2 independent experiments were performed. Data were analyzed by unpaired Student's t test or ANOVA with Tukey's posthoc test and are shown as mean ± SD; *p ≤ 0.05, **p ≤ 0.01, ***p ≤ 0.001.

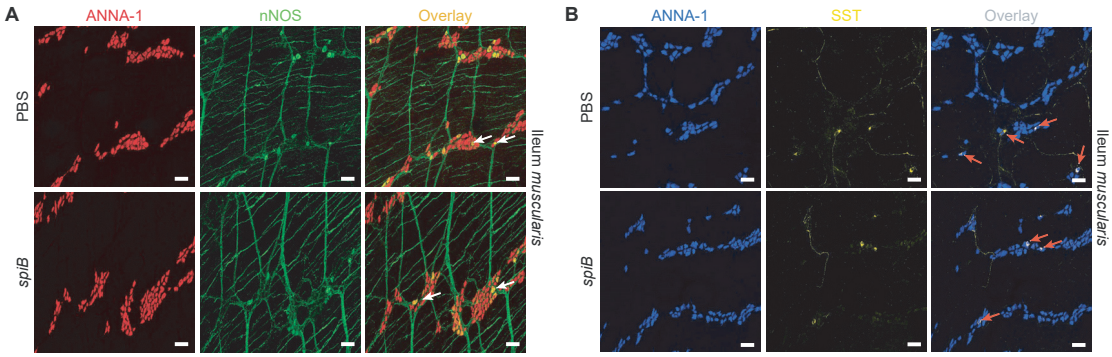

Figure S2. Immunofluorescent Characterization of Inhibitory and Interneuron iEAN Populations Post-*spiB* Infection, Related to Figure 2

(A) Representative confocal immunofluorescence image of ileum myenteric plexus from C57BL/6J stained with anti-ANNA-1 (red) and anti-neuronal nitric oxide synthase (nNOS) (green) antibodies. (B) Representative confocal immunofluorescence image of ileum myenteric plexus from C57BL/6J stained with anti-ANNA-1 (blue) and anti-somatostatin (SST) (yellow) antibodies. Scale bars, 50 μm. Images representative of n = 5 mice.

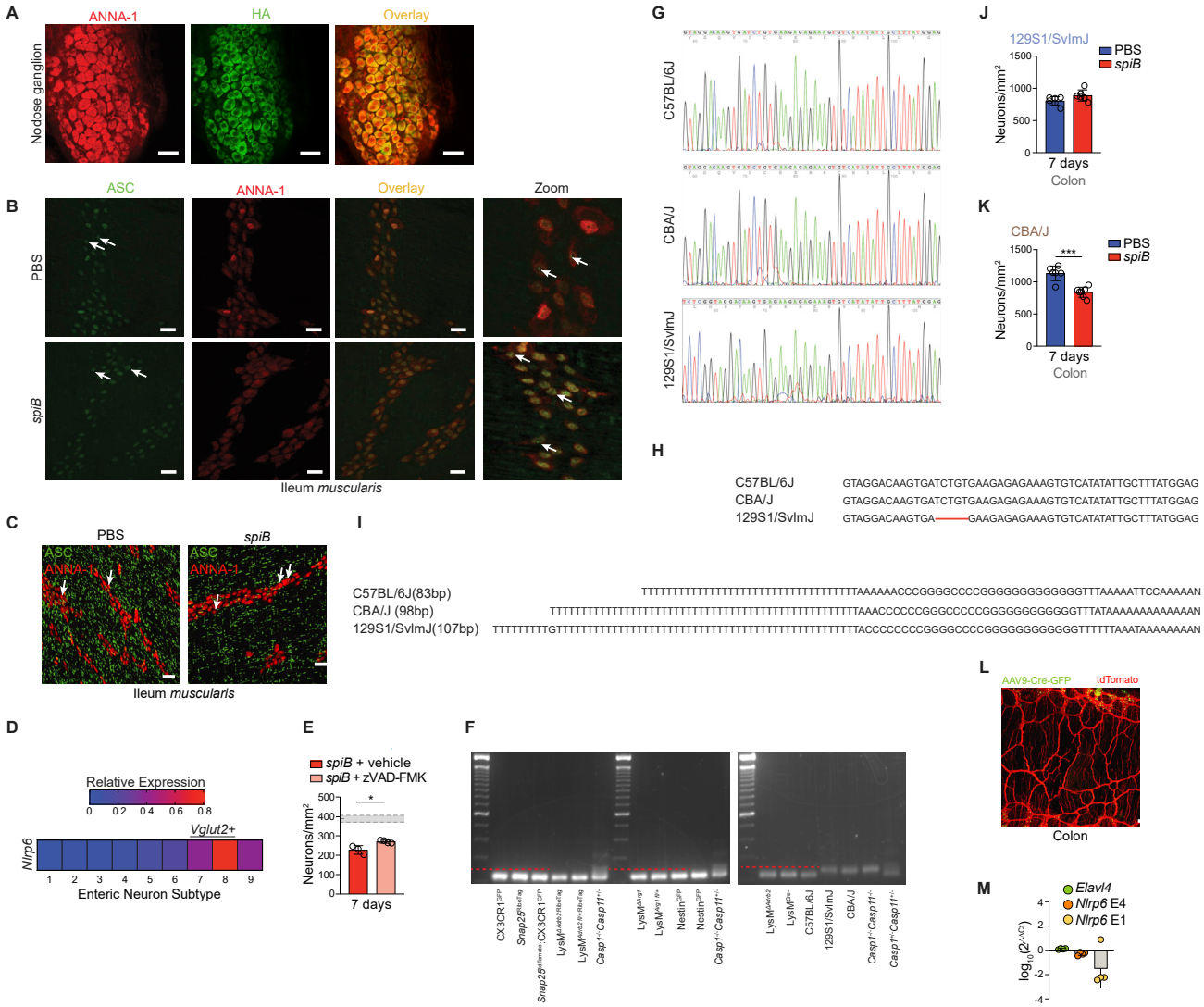

Figure S3. Characterization of RiboTag, and Viral and Genetic Inflammasome Targeting, Related to Figure 3

(A) Representative confocal immunofluorescence images of the nodose ganglia from *Snap25*$^{\text{RiboTag}}$ mice stained with anti-ANNA-1 (red) and anti-HA (green) antibodies. Scale bars, 50 μm. Images representative of n = 5 mice. (B) Immunofluorescence staining of the ileum myenteric plexus from C57BL/6J mice using anti-ANNA-1 (red) and anti-PYCARD (ASC, green) antibodies. Samples obtained 6 h post-oral gavage of PBS or 10^9 CFU of *Salmonella spiB*. Arrows indicate ASC "specks"; inset shows ImageJ zoom of the indicated panel in PBS-treated mice. Scale bars, 25 μm. Images representative of at least n = 5 per group. (C) Immunofluorescence staining of ileum myenteric plexus from ASC$^{\text{mCitrine}}$ mice using anti-ANNA-1 (red) antibody and native mCitrine fluorescence. Samples obtained 5 days post-oral gavage of PBS or 10^9 CFU of *Salmonella spiB*. Arrows indicate ASC "specks" within neurons. Scale bars, 50 μm. Images representative of at least n = 3 per group. (D) Heatmap representation of the relative expression of *Nlrp6* in iEAN subsets as defined by single-cell analysis from the published dataset mousebrain.org/genesearch.html (Zeisel et al., 2018). *Vglut2*+ subsets as defined by the same analysis are highlighted. (E) Neuronal quantification (ANNA-1 staining) in the myenteric plexus of ileal segments on day 7 post-*spiB* infection of C57BL/6J mice receiving vehicle (dimethyl sulfoxide, DMSO) or zVAD-FMK (150 μg/day) delivered i.p. over the course of infection. Shaded area bounded by dashed lines indicates mean day 7 iEAN numbers ± SEM of all control C57BL6/J mice analyzed in Figure 1F. (F-I) Analysis of *Casp11* mutations in mouse strains used. (F) 3% agarose gel for *Casp11* 5bp deletion PCR product. Mouse strains used in this work are indicated below each lane. Red dashed line indicates the size at which a potential 5bp deletion PCR product will run; (G) Sanger sequencing of *Casp11* 5bp deletion PCR product in C57BL/6J, CBA/J, and 129S1/SvImJ mice; (H) Sequence surrounding *Casp11* 5bp deletion region in C57BL/6J, CBA/J, and 129S1/SvImJ mice. Red line indicates 5bp deletion in 129S1/SvImJ mice; (I) Comparison of the length of intron sequences obtained from *Casp11* 5bp deletion PCR product in C57BL/6J, CBA/J, and 129S1/SvImJ mice.(J, K) Neuronal quantification (ANNA-1 staining) in the myenteric plexus of colonic segments on day 7 post-*spiB* infection of (J) 129S1/SvImJ mice and (K) CBA/J mice. (L) Representative confocal immunofluorescence image of the colon muscularis of *Rosa26*$^{\text{lsl-tdTomato}}$ mice given i.v. injection of AAV9-hSyn-Cre-GFP virus. Image representative of at least n = 3. Scale bar, 50 μm. (M) Log transformed relative expression to *Rpl32* of TRAP-qPCR data of *Elavl4* and *Nlrp6* from *Snap25*$^{\Delta Nlrp6:\text{RiboTag}}$ as compared to *Snap25*$^{Nlr6flox/+:\text{RiboTag}}$. Data are representative of 3-5 mice per condition. Data were analyzed by unpaired Student's t test and are shown as mean ± SD; *p ≤ 0.05, ***p ≤ 0.001.

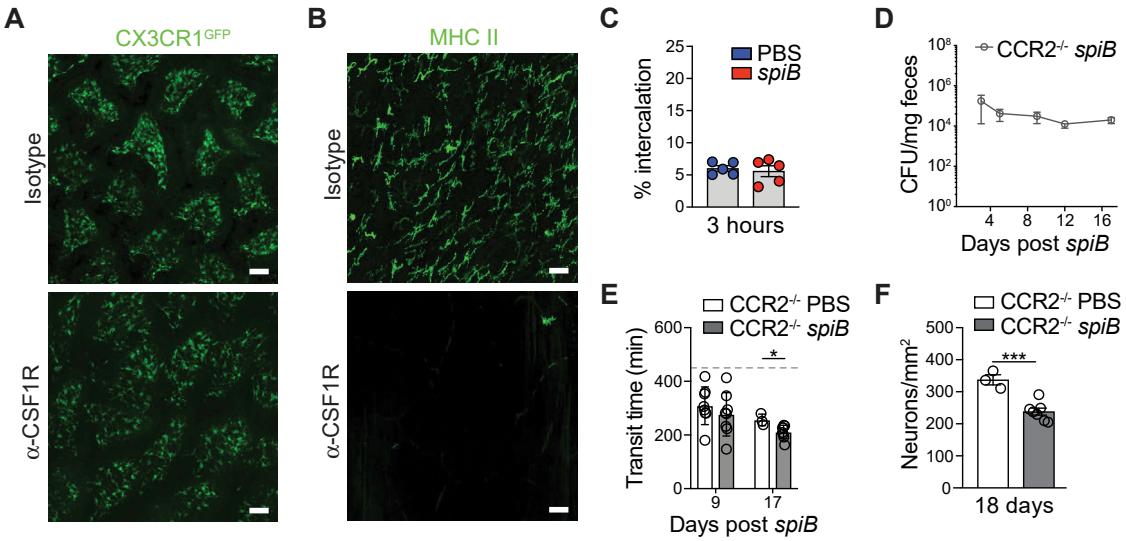

Figure S4. Targeting Validation of Antibody-Mediated MM Depletion and CCR2$^{-/-}$ *spiB* Infection Characteristics, Related to Figure 4

(A) Representative confocal immunofluorescence image of the ileum submucosal layer of *Cx3cr1*^{GFP} mice treated with anti-CSF1R or IgG isotype control antibody by intraperitoneal injections. Scale bar, 50 μm. Images representative of at least n = 3 mice per condition. (B) Representative confocal immunofluorescence image of the ileum myenteric plexus of C57BL/6J mice on day 7 post-treatment with anti-CSF1R or isotype control. Scale bar, 50 μm. Images representative of at least n = 5 mice per condition. (C) Quantification of MM intercalation into ileum myenteric plexus ganglia as assessed by confocal immunofluorescence imaging and calculations based on Imaris software surface functions. Samples obtained at 3 h post-oral gavage of PBS or *spiB*; (D-F) CCR2$^{-/-}$ mice were orally infected with *Salmonella spiB* or gavaged with PBS (D) Quantification of fecal CFU on the indicated days post infection; (E) Gastrointestinal motility activity as assessed by total intestinal transit time on the indicated days post-infection; experiments were ended at 450 min (dashed line); (F) Quantification of neurons of the ileum myenteric plexus as assessed by immunofluorescence staining (ANNA-1). Data are representative of at least n = 4 per condition. At least 2 independent experiments were performed. Data were analyzed by unpaired Student's t test and are shown as mean ± SD (C) or mean ± SEM (D-F); *$p \leq 0.05$, ***$p \leq 0.001$.

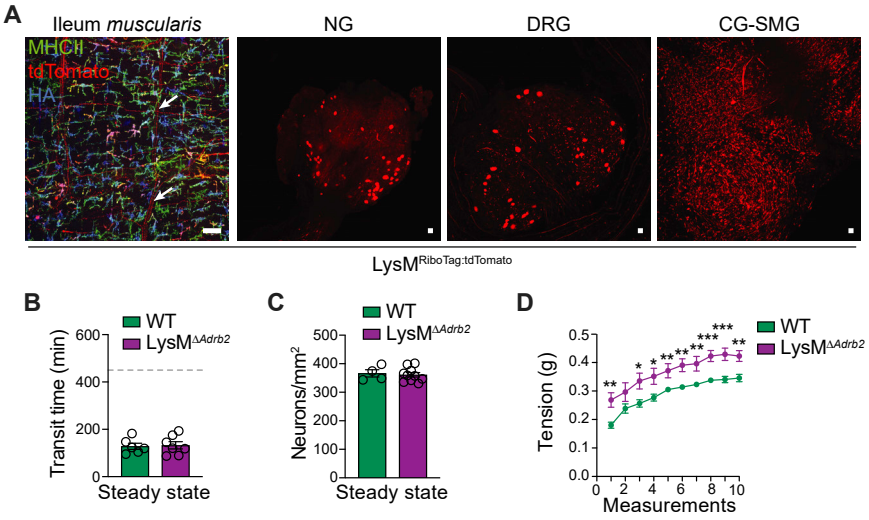

Figure S5. Conditional Targeting of *Adrb2* in MMs Does Not Alter Steady-State Parameters, but Leads to Deficits Post-Infection, Related to Figure 5

(A) Whole-mount IF images of the ileum myenteric plexus, nodose ganglion (NG), thoracic dorsal root ganglion (DRG), and celiac-superior mesenteric ganglion (CG-SMG) from LysM$^{RiboTag:tdTomato}$ mice in the ileum stained for MHC II (green) and HA (blue). Images representative of n = 4. Scale bars, 50 μm. (B) Gastrointestinal motility as assessed by total intestinal transit time of naive LysM$^{\Delta Adrb2}$ and wild-type (WT) littermate control mice; experiments were ended at 450 min (dashed line); (C) Neuronal quantification as assessed by immunofluorescence staining (ANNA-1) in the ileum myenteric plexus of naive LysM$^{\Delta Adrb2}$ and WT littermate control mice; (D) Ileal ring myography assessed on day 53 post-infection of LysM$^{\Delta Adrb2}$ and WT littermate control mice; Data are representative of at least 3 mice per condition. At least 2 independent experiments were performed. Data were analyzed by unpaired Student's t test and are shown as mean ± SD; n.s. – not significant, *p ≤ 0.05, **p ≤ 0.01, ***p ≤ 0.001.

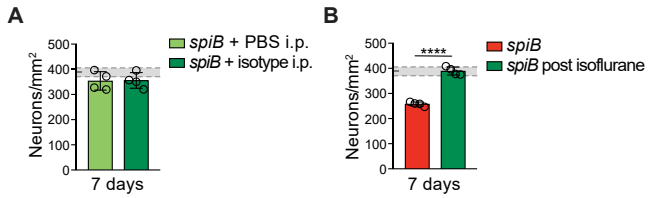

Figure S6. Stress or Anesthetic-Mediated Activation of the Sympathetic Nervous System Can Rescue iEAN Loss, Related to Figure 6

(A, B) Neuronal quantification as assessed by IF staining (ANNA-1) in the myenteric plexus of ileal segments on day 7 post-infection of C57BL/6 with *spiB* (A) receiving mock i.p. injections of PBS or IgG isotype control antibody or (B) following isoflurane anesthesia for 15 min 1 h prior to infection. Shaded area bounded by dashed lines indicates mean day 7 iEAN numbers ± SEM of all control C57BL6/J mice analyzed in Figure 1F; Data are representative of at least 3 mice per condition. At least 2 independent experiments were performed. Data were analyzed by unpaired Student's t test and are shown as mean ± SD; n.s. – not significant, ****$p \leq 0.0001$.

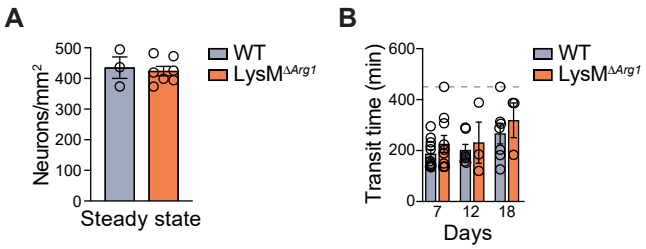

Figure S7. Conditional Targeting of *Arg1* in MMs Does Not Alter Steady-State Parameters, but Leads to Deficits Post-Infection, Related to Figure 7

(A) Neuronal quantification as assessed by immunofluorescence staining (ANNA-1) in the ileum myenteric plexus of naive LysM$^{\Delta Arg1}$ and WT littermate control mice 7 days post–streptomycin treatment (no infection). (B) Gastrointestinal motility activity as assessed by total gastrointestinal transit time at the indicated time points of LysM$^{\Delta Arg1}$ and WT littermate control mice orally infected with 10^9 CFU of *spiB*. Experiments were ended at 450 min (dashed line). Data are representative of at least 3 mice per condition. At least 2 independent experiments were performed. Data were analyzed by unpaired Student's t test and are shown as mean ± SD.